# A New Method for Ice-Ice Aggregation in the Adaptive Habit Model

Kara J. Sulia*

*University at Albany, Albany, New York*

Zachary J. Lebo

*University of Wyoming, Laramie, Wyoming*

Vanessa M. Przybylo

*University at Albany, Albany, New York*

Carl G. Schmitt

*NCAR, Boulder, Colorado*

*currently at the University of Alaska, Fairbanks, Fairbanks, Alaska*



*Corresponding author address: Kara J. Sulia, Atmospheric Sciences Research Center, The University at Albany, 251 Fuller Road, Albany, NY 12203

E-mail: ksulia@albany.edu



**Early Online Release:** This preliminary version has been accepted for publication in *Journal of the Atmospheric Sciences*, may be fully cited, and has been assigned DOI 10.1175/JAS-D-20-0020.1. The final typeset copyedited article will replace the EOR at the above DOI when it is published.

# ABSTRACT





Accepted for publication in *Journal of the Atmospheric Sciences*. DOI 10.1175/JAS-D-20-0020.1.

A novel methodology for modeling ice-ice aggregation is presented. This methodology combines a modified hydrodynamic collection algorithm with bulk aggregate characteristic information from an offline simulator that collects ice particles, namely, the Ice Particle and Aggregate Simulator, and has been implemented into the Adaptive Habit Microphysics scheme in the Weather Research and Forecasting Model. Aggregates, or snow, are formed via collection of cloud ice particles, where initial ice characteristics and the resulting geometry determine aggregate characteristics. Upon implementation, idealized squall-line simulations are performed to examine the new methodology in comparison with commonly used bulk microphysics schemes. It is found that the adaptive habit aggregation parameterization develops snow and reduces ice mass and number concentrations compared to other schemes. The development of aggregates through the new methodology cascades into other interesting effects, including enhancements in ice and snow growth, as well as homogeneous freezing. Further microphysical analyses reveal varying sensitivities, where snow processes are most sensitive to the new parameterization, followed by ice, then cloud, rain, and graupel processes. Further, the new scheme results in enhancements in surface precipitation due to the persistence of snow at lower altitudes. This persistence is a result of shape-dependent melting and sublimation, increasing the residence time. Moreover, these low-level enhancements are reflected in increases in radar reflectivity at the surface and its spatial distribution. Finally, the ability to predict snow shape and density allows for the simulation of polarimetric radar quantities, resulting in signature enhancements compared to schemes that do not consider spatial and temporal variations in snow shape and density.



Accepted for publication in *Journal of the Atmospheric Sciences*. DOI10.1175/JAS-D-20-0020.1.

## 1. Introduction

The development of most precipitable hydrometeors relies on the growth of ice crystals. Bergeron presented at the International Union of Geodesy and Geophysics (IUGG) conference in 1933 (Braham 1968) the hypothesis that most rain drops are derived from ice crystals in supercooled clouds. Subsequent research (e.g., Houghton 1950) indicated that within the midlatitudes, a combination of the Wegener-Bergeron-Findeison (Wegener 1911; Bergeron 1935; Findeisen 1938, WBF hereafter) process and the growth via collection are required for the production of precipitation-sized rain drops, and that if ice crystals are present, precipitation development is dominated by ice-crystal growth processes rather than by warm-phase collision-coalescence. Houghton (1950) extend the collection possibilities to growth via "clumping of snowflakes," depositional growth of ice crystals that melt and then grow through warm accretion, and the formation of graupel.

The growth of ice crystals through vapor deposition is a fundamental and necessary mechanism for ice crystal evolution and at times sufficient to develop precipitation-sized hydrometeors in shallow wintertime convection. However, precipitation in deeper convective environments wherein hydrometeors must reach appreciable speeds, and thus sizes, to sediment, cannot grow through vapor deposition alone. To this point, the WBF process dominates as a critical catalyst for the formation of precipitation until the crystals achieve terminal velocities similar to those of drizzle, at which point this process becomes secondary to collection processes, such as aggregation and riming (Houghton 1950).

Aggregation is the process by which two or more individual or aggregated ice crystals join, which can occur in any cloud in which ice crystals are present; aggregates are especially prevalent in clouds that are sufficiently deep to encompass several temperature regimes. Aggregates can develop at any altitude and be advected into multiple regions. Areas where ice particles can





Accepted for publication in *Journal of the Atmospheric Sciences*. DOI10.1175/JAS-D-20-0020.1.

become dendritic allow for collection through interlocking (Rogers and Yau 1989); this interlocking is also prevalent for bullet-rosettes, which occur at temperatures $\leq -30°$C and are common in cirrus. However, Braham (1968) indicated that aggregation is most prevalent at temperatures of $0-10°$C, echoing Hosler et al. (1957) in that the likelihood of aggregation increases as temperatures increase toward 0°C, becoming negligible for temperatures $< -25°$C. Warmer dendritic temperatures ($T \approx -12°$C) not only result in ice particles with branching arms amenable to interlocking (Phillips et al. 2015) but are also theorized to be associated with a quasi-liquid layer[1] on ice crystal surfaces (Kuroda and Lacmann 1982), effectively increasing the "stickiness," indicating a dependency for collection efficiency on both temperature and particle size, as formulated by Phillips et al. (2015). This can occur for any particle formed at low temperatures that falls into warmer regions. This process is most effective in mid-latitude cloud systems with relatively low liquid water contents (LWCs), reducing mass loss due to warm-phase precipitation, increasing cloud lifetime, and enabling the persistence of cold-phase growth processes. Such systems can produce many frozen hydrometeors with high sedimentation rates, affecting not only the precipitation rate at the surface but also the phase partitioning within the cloud and scattering properties at cloud top due to the loss of larger and less pristine ice crystals.

The effect of non-spherical ice-ice aggregation is explored herein. Minute intricacies associated with ice growth from vapor deposition were explored through development of the adaptive ice habit model in Harrington et al. (2013a). This work extends such development to include the effect of non-spherical ice-ice aggregation and is analyzed herein. While a number of investigations of processes affected by the non-spherical growth of ice crystals have followed the development of the adaptive habit model (AHM, Harrington et al. 2013b; Sulia et al. 2013, 2014; Sulia and Kumjian 2017a,b; Jensen et al. 2017, 2018b,a; Harrington et al. 2019; Gaudet et al. 2019), includ-

[1]Note that this thermodynamic effect does not account for the maximum in sticking efficiency at temperatures observed in the lab (e.g., -16°C).



Accepted for publication in *Journal of the Atmospheric Sciences*. DOI10.1175/JAS-D-20-0020.1.

ing the development of a riming scheme (Jensen and Harrington 2015), detailed investigations of the impact of ice habit on aggregation are lacking. Hence, a novel methodology is employed for the representation of snow via ice-ice aggregation. This work builds upon that of Przybylo et al. (2019) and the extension of the Ice Particle and Aggregate Simulator (IPAS, Schmitt and Heymsfield 2014) to first establish a robust database of aggregrate properties, which is then integrated into the AHM. A description of the models and new methodology are outlined in the following section. Upon integration, idealized squall-line simulations are performed to assess the microphysical sensitivities of the new ice-ice aggregation scheme and cascading effects. Further idealized investigations are performed to understand the impacts of the new scheme on resulting modeled surface precipitation and polarimetric radar signatures. This investigation concludes with summary remarks and intentions for future work.

## 2. Model Description and Methodology

A new methodology for modeling ice-ice aggregation has been developed adhering to AHM specifications. The growth of ice from vapor is computed within the AHM, the shape and size of which are then used as inputs to IPAS. IPAS then computes resulting aggregate shape, size, and density information. Separately, a modified hydrodynamic collection kernel is used to compute aggregate mass and number. Both techniques are offline and used to populate lookup tables then implemented into the AHM for the prediction of aggregates. This methodology is described below, following a brief overview of the AHM.

### *a. Adaptive Habit Model (AHM)*

Hydrometeors are assumed to be spherical within many commonly used microphysical schemes. In some cases, ice particles and snow are parameterized to follow an equivalent volume method



Accepted for publication in *Journal of the Atmospheric Sciences*. DOI10.1175/JAS-D-20-0020.1.

with a fixed density (e.g., Lin et al. 1983; Reisner et al. 1998; Thompson et al. 2004; Morrison et al. 2009) or assume ice particle shape *a priori* according to temperature using mass-dimensional relationships (e.g., Koenig 1971; Walko et al. 1995; Woods et al. 2007; Thompson et al. 2008). Although these methods may be appropriate for liquid hydrometeors (rain and cloud drops), and in some frozen cases outside of habit-prone regimes, these methods diagnose the evolution from predefined parameters and do not allow for the nonlinear evolution of particle shape with growth and hence are unable to capture the detailed growth (mass and size) and advective history of these particles. This deficiency can cascade into incorrect predictions of liquid and ice masses and ice sedimentation (e.g., Harrington et al. 2013a; Sulia et al. 2014), collection efficiency (e.g., Ono 1969; Hall 1980; Jensen and Harrington 2015), optical depth and scattering properties (e.g., Takano and Liou 1989; Key et al. 2002), surface precipitation (e.g., Gaudet et al. 2019), subsequent radar estimates of reflectivity and other polarimetric quantities (e.g., Sulia and Kumjian 2017a), etc.

The depositional growth of ice crystals depends on the local temperature and saturation as well as the existing particle shape, size, and density, all of which evolve nonlinearly (Sulia and Harrington 2011). The backbone of the AHM is based in crystal growth theory, employing inherent growth ratios (IGRs)[2] from Chen and Lamb (1994) for $-20 \leq T \leq 0$°C, accounting for the predictable planar-columnar oscillations with temperature, and from Hashino and Tripoli (2008) for $-60 \leq T \leq -20$°C, accounting for columnar polycrystalline habits. The AHM tracks the growth history of the bulk parameters needed to predict ice crystal aspect ratio ($\phi$), allowing for an effective means of evolving particle shape and mass in a physically consistent manner. This tracking method is required to accurately predict the ice and liquid water contents in mixed-phase clouds (Harrington et al. 2013a,b). The method has been derived from and validated against a detailed

[2]IGR is a function of temperature and defines the ratio of vapor deposition along the two particle axis lengths, controlling the primary habit (aspect ratio).



Accepted for publication in *Journal of the Atmospheric Sciences*. DOI10.1175/JAS-D-20-0020.1.

bin ice growth method (Harrington et al. 2013b), which stems from Chen and Lamb (1994) and compares well to wind-tunnel laboratory-grown particles (Fukuta and Takahashi 1999). The microphysical method has been tested on an Eulerian grid within a two-dimensional kinematic model (Sulia et al. 2013). The dynamical impacts of the adaptive habit approach have been explored within the Weather Research and Forecasting (WRF) model for large eddy simulations (LES, Sulia et al. 2014), indicating the indirect effects of crystal habit growth on the dynamic collapse of mixed-phase clouds. Further, with the ability to predict and evolve particle aspect ratio and density, investigations of the impact of ice crystal habit on resulting polarimetric quantities and microphysical sensitivity thereof are presented in Sulia and Kumjian (2017a) for an idealized WRF-LES case and in Sulia and Kumjian (2017b) for an orographic snow storm in the Front Range of the Rocky Mountains, indicating that AHM reflectivity magnitudes are similar to those observed with radar and are an improvement over spherical ice crystal assumptions.

The AHM predicts ice mass $q_i$, number $n_i$, and axis length-weighted spheroidal-volume ($a_{iv}$ and $c_{iv}$, needed to advect axis lengths while conserving density) mixing ratios following Harrington et al. (2013a) and Jensen et al. (2017), where $n_i$ is determined according to a modified gamma distribution of the $a$ axis. In addition to ice, the AHM predicts the mass mixing ratio for liquid cloud droplets $q_c$, where the number concentration of cloud drops is computed as a gamma distribution following Morrison and Grabowski (2007) with $N_c = 250$ cm$^{-3}$. The model also predicts mass and number mixing ratios for rain ($q_r$ and $n_r$) and graupel ($q_g$ and $n_g$, respectively), where $n_r$ and $n_g$ are related to the slope and intercept parameters assuming an exponential distribution (for details see Morrison et al. 2009, 2012). Snow ($q_s$ and $n_s$) is also included and is the topic of this paper as presented below.

The AHM was initially developed and tested extensively for the depositional growth of individual ice crystals (monomers). The development of more complex microphysical processes needed



Accepted for publication in *Journal of the Atmospheric Sciences*. DOI10.1175/JAS-D-20-0020.1.

for universal cloud applications is ongoing for the AHM, including the development of methodologies for riming and aggregation of vapor-grown ice crystals. Riming has been completed by Jensen and Harrington (2015) and validated thereafter (Jensen et al. 2017, 2018b,a); however, the implementation of this scheme is complex and outside the scope of this work, and so the "traditional" two-moment methodology (Morrison et al. 2009) indicated above is employed.

Presented herein is a novel method for ice-ice aggregation developed with the specific monomer and aggregate characteristics that are required for seamless integration within the AHM, as described below. Note that while the focus of this work is on extension of the AHM to include shape-specific aggregation, given the offline nature and general amenability of IPAS, integration into other microphysical schemes that account for ice crystal shape, such as a bin model (Khain et al. 1989, albeit habit is not prognostic but predefined in this scheme), is also possible.

*b. Ice Particle and Aggregate Simulator (IPAS)*

Because the AHM allows for the evolution of non-spherical ice crystals during deposition, sublimation, and melting, aggregation must take into account the dimensional characteristics of these particles. Further, as the intent of the AHM is to reduce the arbitrary nature in which ice particle properties are defined, the aggregation methodology designed herein allows for the prediction of bulk aggregate dimensional and density information upon formation. The way in which aggregates are formed from ice is extremely complicated given the many geometrical factors to consider during aggregation (e.g., overlap, contact angle, falling orientation, offset—or rotation in the horizontal, etc.). There is no economical way to simulate this process in a statistically significant sense (generating many thousands of aggregate scenarios) using traditional modeling techniques (e.g., bin/bulk models or computational fluid dynamical simulations) without including a myriad of assumptions. Hence, the work presented herein employs a numerical tool to permit simula-



Accepted for publication in *Journal of the Atmospheric Sciences*. DOI10.1175/JAS-D-20-0020.1.

tions of numerous interactions between ice crystals of various shapes, sizes, and geometries in a highly controlled environment. Namely, the Ice Particle and Aggregate Simulator (IPAS) serves as a "theoretical" laboratory in which to simulate aggregation and is advantageous in this work as it allows for computational efficiency and the ability to control for all free parameters.

IPAS was initially developed by Schmitt and Heymsfield (2010, 2014) and recently refactored[3] and extended by Przybylo et al. (2019) for the purposes of this work. IPAS is an offline box model that uses hexagonal prisms (or any specified geometry) to simulate the aggregation of ice crystals. The hexagonal prisms are defined with an equivalent volume spherical radius and aspect ratio to represent the primary habits of either plates or columns. Two identical prisms, or monomers, are either oriented so that the projected area from above is maximized (particles falling quasi-horizontal) or randomly oriented. The two monomers then collide under the constraints of random overlap, offset, and contact angle (in the case of random falling orientation[4]). Once collected, the aggregate characteristics are computed, including aggregate aspect ratio and major and minor dimensions. The aggregate major and minor dimensions are determined as the maximum and minimum dimensions of the circumscribing ellipsoid, respectively. Other parameters are extracted as well, such as the 2-dimensional aspect ratio (Jiang et al. 2017) and complexity (Schmitt and Heymsfield 2014). The former characteristics are required for AHM implementation, whereas the latter are compiled for comparisons to other aggregation schemes and observations (e.g., ice particle probe images). This process is completed 300 times (i.e., 300 aggregates are formed, a number determined to provide robust results). These 300 aggregate variations (made up of identical monomers each) are used to fill a distribution, defined by the extracted parameter of interest (e.g., aspect ratio) and subsequently fit by a gamma distribution, from which the characteristic, or the mode of the distribution, is obtained, as well as the distribution mean. This approach is critical

[3]Refactoring is the process of programmatically redesigning the model to improve efficacy without compromising intended functionality.
[4]Note that for the simulations herein, only the quasi-horizontal orientation is considered.



Accepted for publication in *Journal of the Atmospheric Sciences*. DOI10.1175/JAS-D-20-0020.1.

for implementation into a *bulk* microphysics scheme, and knowing both the mean and characteristic values allows for determination of the bulk gamma distribution shape within the AHM.

The process outlined above and detailed in Przybylo et al. (2019) is repeated for 20 monomer equivalent volume spherical radii $r_{eq}$ (logarithmically spaced from 0.01 to 100) and 28 aspect ratios $\phi$ (logarithmically spaced across 3 orders of magnitude). The result is a database of necessary characteristic and mean values of resulting bulk aggregate $a$ and $c$ axes for predefined monomers characterized by $r_{eq}$ and $\phi$. Bulk monomer $r_{eq}$ and $\phi$ are predicted by the AHM and can therefore be used as input parameters to this database to determine the bulk characteristics of aggregates formed via collisions between individual ice crystals in the AHM. Similar to ice growth and evolution, aggregates (or snow) are defined by their $a$ and $c$ axes, from which other parameters can be derived. Thus, the parameterization scheme in which ice crystals are advected and changed through vapor deposition, sublimation, and/or melting are used to parameterize these same processes for snow given analogous parameters.

In addition to the $a$ and $c$ axes, the secondary habits[5] in the AHM are parameterized through the prognostic evolution of ice density, which is reduced for non-spherical crystals. Aggregates, too, have a reduced density, traditionally assumed to be 100 kg m$^{-3}$. With the desire to avoid assumptions, IPAS is used to characterize bulk aggregate density as well.

IPAS particles are collected in a domain that is measured in arbitrary dimensions (e.g., pixels) and there is no mass quantity; density evolution is accomplished by calculating the density change after aggregation. This change is computed by determining the ratio of the initial monomer volume relative to the smallest initial ellipsoid volume that circumscribes that monomer. That initial ratio is then compared to the ratio of the aggregate volume to the smallest ellipsoid volume that circumscribes the aggregate. In both cases, the ratio defines the fraction of the ellipsoid that is

[5]Primary habits are determined by temperature (IGR) and defined by aspect ratio $\phi = \frac{c}{a}$ (e.g., plate or column), and secondary habits are determined by saturation and defined by density $\rho_i$ (e.g., dendrite or needle).



Accepted for publication in *Journal of the Atmospheric Sciences*. DOI10.1175/JAS-D-20-0020.1.

comprised of the crystal, providing a measure of density. A change in density is then determined from the difference between the initial and final densities, and a database of the bulk density distribution characteristic values is similarly recorded (because this too is computed for each of the 300 aggregate realizations per $r_{eq}$ and $\phi$ pair).

The aforementioned bulk characteristic parameters are compiled into lookup tables for the implementation of ice-ice aggregation in the AHM. This look-up table approach enables the ability to maintain computational efficiency while still including the necessary physics and is becoming an increasingly common approach (e.g., Jensen and Harrington 2015; Morrison and Milbrandt 2015) for variables the modeling of which remains intensive.

Aggregate characteristics formed from non-spherical monomers are generated through the creation of a massive ($20 \times 28 \times 300 = 168{,}000$ in this case) database of simulated aggregates in IPAS, as described above and in detail in Przybylo et al. (2019). The computational expense required to generate these data is beyond that to be reasonably represented directly within the AHM, i.e., implementing IPAS directly into the AHM would be far too computationally expensive. For the same computational reasons, 3D fluid flow and trace trajectories are neglected in IPAS given the sample size of formed aggregates. While IPAS is a useful tool for the formation of aggregates and the characterization of geometrical aggregate properties, this offline 'theoretical laboratory' is idealized and unable to carry with it information on mass and number. Therefore, a separate lookup table is generated for these quantities, discussed next.

*c. Mass and Number*

IPAS is unable to predict or evolve the mass and number of particles during the aggregation process, which is required for computations of aggregation in numerical models. Particularly for this work, *shape-dependent* mass and number computations are required. As such, a modified



Accepted for publication in *Journal of the Atmospheric Sciences*. DOI10.1175/JAS-D-20-0020.1.

collection equation has been developed that allows for collection of non-spherical particles over a large range of aspect ratios in a bulk sense. This methodology for collection relies on the hydrodynamical collection kernel (e.g., Pruppacher and Klett 1997) but is extended for the purposes of this work to represent non-spherical hydrometeors. Thus, instead of having a single variable representing the size of the collected and collector ice crystals, i.e., radius or diameter, two variables are needed, namely the $a$ and $c$ axes of each crystal. With this, the bulk rate of change of the mass mixing ratio (kg kg$^{-1}$ s$^{-1}$) due to the aggregation of two ice crystal populations (denoted by $x$ and $y$ subscripts) can be defined as follows:

$$dm_{xy} = \frac{\pi}{\rho_a} \int_{a_{x_{min}}}^{a_{x_{max}}} \int_{c_{x_{min}}}^{c_{x_{max}}} \int_{a_{y_{min}}}^{a_{y_{max}}} \int_{c_{y_{min}}}^{c_{y_{max}}} \rho_i V_{xy} A |v_x - v_y| N_x N_y E dc_y da_y dc_x da_x. \tag{1}$$

This quantity determines the amount of mass removed from the ice mass mixing ratio and added to the snow mass mixing ratio. Area $A$ is $[max(a_x, c_x) + max(a_y, c_y)]^2$, $v_x$ and $v_y$ follow the pressure-dependent terminal velocity equations developed in Heymsfield et al. (2013) for clouds designated as stratiform (their Equations 11a-c), $E$ is the collection efficiency, $V_{xy} = (a_x^2 c_x + a_y^2 c_y)$, $\rho_i$ is the ice density, and $\rho_a$ is air density. As already implemented in the AHM, it is assumed that the monomers are distributed via a gamma distribution:

$$N_z = \frac{N_t}{\Gamma(\nu)} \left(\frac{l_z}{l_n}\right)^{\nu-1} \frac{1}{l_n} \exp\left(-\frac{l_z}{l_n}\right), \tag{2}$$

where $l = a$ or $c$, $z = x$ or $y$, $N_t$ is the total number of particles in the gamma ($\Gamma$) distribution with shape $\nu$ and characteristic size $l_n$. The ranges of $l_z = a_x$, $c_x$, $a_y$, $c_y$ are identical and logarithmically spaced from $l_{z_{min}} = 0.5$ $\mu$m to $l_{z_{max}} = 10$ mm.



Accepted for publication in *Journal of the Atmospheric Sciences*. DOI10.1175/JAS-D-20-0020.1.

The above equation is computed for each of the following inputs: $N_t = 1$, 10, 100, 1000, 10000 $L^{-1}$, $a_n = 1$, 10, 100, 1000, 10000, 100000 $\mu$m, $c_n = 1$, 10, 100, 1000, 10000, 100000 $\mu$m, $\nu =$ 1-8, and $\rho_i =$ 100-900 kg/m$^3$. A 5-dimensional lookup table is therefore generated, which is then integrated into the AHM. Given the above, the only parameter that remains set *a priori* through this methodology is $E$, which follows that of Connolly et al. (2012), with values of 0.09, 0.21, 0.6, 0.1, 0.08, 0.02 for $T = -5$, -10, -15, -20, -25, -30°C, respectively. $E$ is set to 0.09 when $T > -5$°C, 0.02 when $T < -30$°C, and linearly interpolated otherwise. These values are deemed appropriate by Connolly et al. (2012) particularly within the beginning stages of aggregation, which is the situation here where only ice-ice aggregation is considered. Note that while more recent and advanced algorithms exist for computations of sticking efficiency (e.g., Phillips et al. 2015), the implementation of an advanced efficiency scheme is outside the scope of this work, but will be considered in the future.

## 3. Model Setup

This work implements bulk aggregate characteristics using an offline simulator, IPAS. The results presented herein are idealized and are meant to illustrate the new ice-ice aggregation methodology implemented into the AHM as well as the combined influence of the original vapor-growth model and the new aggregation scheme. While idealized, the purpose of this study is to determine the model's ability to produce vapor-grown microphysical signatures and their subsequent self-collection. This work provides a basis for more complex case studies, where signatures may be convoluted by the effects of other processes. More realistic simulations will be explored in subsequent work.



Accepted for publication in *Journal of the Atmospheric Sciences*. DOI10.1175/JAS-D-20-0020.1.

*a. Case Description*

The idealized case presented herein is based on the May 20, 2011 squall line observed during the Midlatitude Continental Convective Clouds Experiment (MC3E, Jensen et al. 2016; Xue et al. 2017; Kacan and Lebo 2019). The squall-line simulation is initialized with a sounding based on 1200 UTC observations in Morris, Oklahoma (Fig. 1, right), when the environment is nearly saturated below 700 mb and there is approximately 2200 J $kg^{-1}$ of moist unstable convective available potential energy. As in Kacan and Lebo (2019), modifications to the wind profile (0.003 $s^{-1}$ unidirectional shear from the surface to 4 km, i.e., 12 m $s^{-1}$ at the surface decreasing to 0 m $s^{-1}$ at a height of 4 km) were employed to ensure squall-line formation.

*b. Model Configuration*

This study is simulated using WRFV3.9 with 500 $\times$ 122 horizontal grid points ($\Delta x = \Delta y = 1$ km) and 100 hyperbolic vertical grid points reaching an altitude of 24 km ($\Delta z = 202 \sim 465$ m). Boundary conditions are open in the $x$-direction (perpendicular to the line of convection) and periodic in the $y$-direction (parallel to the line of convection). Turbulent diffusion is determined from the 1.5-order TKE closure. The model is run for 3 h with a 5 s time-step. Three microphysical schemes are simulated: the Morrison two-moment (M2M, Morrison and Grabowski 2010), Thompson (THOM, Thompson et al. 2008), and the original AHM (Harrington et al. 2013a,b). Both M2M and THOM are simulated "out-of-the-box." Additionally, three variations of the AHM are simulated:

1. AHM-ICE-ONLY: Ice grows via vapor deposition alone and can reach sizes of large monomer crystals. There is no snow category and no collection or accretion onto ice; however, note that ice can be collected by rain.



Accepted for publication in *Journal of the Atmospheric Sciences*. DOI10.1175/JAS-D-20-0020.1.

2. AHM-AGG-ORIG: As in Sulia and Kumjian (2017a,b), the ice-to-snow autoconversion threshold (125 $\mu$m) method (for details see Morrison et al. 2009, 2012) is employed for the development of aggregates (see Passarelli 1978; Reisner et al. 1998; Morrison et al. 2009). Autoconversion calculations are then assumed to determine the ice-ice aggregation rate of forming snow once the autoconversion threshold is met; the ice crystals that do not aggregate remain as $q_i$, and so at no point are larger monomer ice crystals autoconverted to snow. Snow (aggregates) can also self-collect (snow-snow aggregation), but the collection of ice crystals by snow (ice-snow aggregation) is not considered. Ice properties are then recalculated to account for the loss of mass and number to snow, and the newly formed aggregates are assumed to be spheres with a density of $\rho_s = 100$ kg m$^{-3}$. Snow ($q_s$ and $n_s$) is an aggregate category only (thus contains no monomer particles) and is separate from cloud ice ($q_i$), which is a monomer category only. Other processes include collection of snow by rain above freezing, accretion of cloud droplets onto snow/graupel, rime splintering, and deposition, all of which follow the M2M parameterizations.

3. AHM-AGG-IPAS: New methodology as described in Sec. 2b. Ice crystals become snow only through ice-ice aggregation; i.e., ice cannot be collected from existing aggregates (snow), and snow cannot self-collect, though this development is ongoing. Snow $q_s$ and $n_s$ are derived from Eqn. 1, and $a_s$, $c_s$, and $\rho_s$ are derived from IPAS (Przybylo et al. 2019). Snow/aggregate deposition is included and analogous to ice deposition in the AHM, where aggregate $a$ axis ($a_s$), $c$ axis ($c_s$), aspect ratio $\phi_s$, and density $\rho_s$ are predicted and evolved. There is no accretion onto ice or snow/aggregates. As in AHM-AGG-ORIG, snow ($q_s$ and $n_s$) is an aggregate category only, contains no monomer particles, and is separate from ice ($q_i$ and $n_i$), which contains only single monomer ice crystals.



Accepted for publication in *Journal of the Atmospheric Sciences*. DOI10.1175/JAS-D-20-0020.1.

For all AHM simulations, ice nucleation follows from Ovchinnikov et al. (2014), only activating when the ice supersaturation reaches 5% and at temperatures $\leq -5°$C. Ice is activated by relaxing the ice number mixing ratio $n_i$ to a steady-state with a maximum prescribed value, $N_i$, set to 1 $\mathrm{L}^{-1}$. This work is to explore the effects of the new aggregation scheme on subsequent processes, and so detailed nucleation is not considered. Microphysical processes involving cloud, rain, and graupel are modeled as in Morrison et al. (2009), unless stated otherwise above. Melting of both ice and snow/aggregates follow the ice and graupel melting scheme in Jensen et al. (2017), and all liquid cloud and rain drops are assumed to homogeneously freeze as spherical ice when $T \leq -40°$C (note that this is an idealized assumption, where a fraction of these drops would evaporate rather than freeze, according to Phillips et al. 2007).

The idealized squall-line simulation is opted as the system encompasses multiple temperature regimes and environments conducive to many microphysical processes and hydrometeor types. This is particularly important for this analysis for the initiation of ice growth through vapor deposition as well as subsequent collection processes and phase change (melting to rain). However, it is important to note that the purpose of this investigation is not to assess the ability for the new scheme to accurately simulate this case, but rather to explore the microphysical phase space resulting from the variations among the schemes described above. A limitation of this presentation is that subsequent collection processes are not considered. While this work is underway, investigation of the microphysical sensitivity to this new methodology of ice-ice aggregation is a critical first step prior to considering more complexity; i.e., the sensitivity to ice-ice aggregation may otherwise be obfuscated by subsequent collection.





Accepted for publication in *Journal of the Atmospheric Sciences*. DOI10.1175/JAS-D-20-0020.1.

## 4. Results

The idealized squall-line simulation described above is completed to assess the new ice-ice aggregation scheme in the AHM. First, a microphysical overview is performed to illustrate how the schemes differ over time and in the vertical, compared to commonly used WRF microphysics options, M2M and THOM. Then, a more thorough microphysical analysis of the AHM schemes is completed to understand the relative sensitivity and significance of microphysical processes due to differences in aggregation parameterization. Finally, contributing factors to surface precipitation are discussed, followed by a brief introduction to the effect of the new scheme on the simulation of polarimetric quantities.

### *a. Microphysical Analysis*

A microphysical analysis is conducted to assess the impact of the new aggregation scheme on the AHM as well as to compare with existing, commonly used bulk microphysics schemes. As such, comparisons are made among AHM-ICE-ONLY, AHM-AGG-ORIG, and AHM-AGG-IPAS, and, when possible, comparisons are also made with M2M and THOM due to similarities in many process parameterizations. Recall the following points: (1) AHM-ICE-ONLY does not contain a snow/aggregate category, only cloud ice; (2) all three AHM schemes model cloud, rain, and graupel processes after those in M2M, except melting, which is modeled after Jensen et al. (2017); (3) AHM-AGG-ORIG snow is partially modeled after M2M (see Sulia and Kumjian (2017a) for details); and (4) AHM-AGG-IPAS snow/aggregates form via ice-ice collection only.

First, Fig. 2 provides a broad overview of the schemes with respect to hydrometeor mass, displaying simulation-averaged (domain and time) mass mixing ratios for AHM-ICE-ONLY (gold), AHM-AGG-ORIG (green), AHM-AGG-IPAS (red), M2M (blue), and THOM (purple). As compared to AHM-ICE-ONLY, all schemes predict less ice, more snow, and more rain; when ag-



Accepted for publication in *Journal of the Atmospheric Sciences*. DOI 10.1175/JAS-D-20-0020.1.

gregation is considered, snow mass increases at the expense of the ice mass, and with larger fall speeds is more likely to reach the melting level and form rain. Other than M2M (total $q_c \approx 8.4 \times 10^{-6}$ kg/kg), all schemes also predict a lower cloud droplet mass than AHM-ICE-ONLY (total $q_c \approx 8.1 \times 10^{-6}$ kg/kg, Fig. 2), although the differences do not exceed $\approx 6 \times 10^{-7}$ kg/kg. The lack of snow in AHM-ICE-ONLY reduces the production of rain through melting and collision coalescence and other cascading processes such as accretion.

The patterns in Fig. 2 follow those in Fig. 3. Time series of spatially averaged mixing ratios are shown in Figs. 3a-e, and vertical profiles of horizontally and temporally averaged mixing ratios in Figs. 3f-j. The first signature to note in Fig. 3 is the large amount of ice produced by AHM-ICE-ONLY (Fig. 3c,h, gold line) both in the vertical and over time, which is due to the lack of aggregation and hence formation of snow and removal via precipitation; again, recall that AHM-ICE-ONLY contains only pristine ice, including what would be considered large snowflakes but formed solely via vapor deposition. When compared to AHM-AGG-ORIG (green) and AHM-AGG-IPAS (red), it is clear that the aggregation of ice crystals to form snow reduces $q_i$ substantially, as expected. This is similarly evident in Fig. 4, where the large ice magnitude in AHM-ICE-ONLY (Fig. 4k) is split between ice and snow in AHM-AGG-ORIG (Fig. 4l,q) and AHM-AGG-IPAS (Fig. 4m,r). In fact, the spatially averaged snow magnitudes are quite similar for AHM-AGG-ORIG and AHM-AGG-IPAS (Figs. 2 and 3d). However, AHM-AGG-ORIG and AHM-AGG-IPAS differ in their vertical distributions of snow (Figs. 3i and 4q,r), where AHM-AGG-ORIG trends follow those of the M2M and THOM schemes, with peaks in mass near 8-9 km, decreasing to $< 0.001$ g/kg at 3 km. In contrast, the vertical distribution of snow in AHM-AGG-IPAS peaks at higher altitudes (Fig. 3i, 11.5 km) with a steady decline all the way to the surface.



Accepted for publication in *Journal of the Atmospheric Sciences*. DOI 10.1175/JAS-D-20-0020.1.

The differences at lower altitudes are a result of the differences in melting and sublimation schemes, which are shown in Fig. 5 along with other processes. Unlike AHM-AGG-ORIG (green), AHM-AGG-IPAS (red) takes into account the shape of snow hydrometeors during melting (Fig. 5j, dashed lines) and sublimation (Fig. 5i). Recall that snow is assumed spherical in all schemes except AHM-AGG-IPAS, and the formation of aggregates via ice crystals is highly dependent on crystal shape. Figure 6 displays vertical profiles of the *a* and *c* axis lengths for AHM-ICE-ONLY (gold, ice only), AHM-AGG-ORIG (green, ice only), and AHM-AGG-IPAS (red, ice and snow/aggregates). A corresponding temperature profile is also shown (Fig. 6, left) with 0, -15, and -40°C isotherms. As the temperature approaches 0°C, a large spike in the ice crystal size results, particularly the *c* axis (temperatures near freezing are preferential to columnar growth). Just above this spike (∼4.25 km) depositional growth of ice and snow begin to drop significantly (Figs. 5g,h, solid) and sublimation (Figs. 5h,i, dashed) dominates. In response, the ice mass (Fig. 3h) drops significantly as well, resulting in an Ostwald ripening effect, wherein only the largest ice crystals remain and grow at the expense of the smaller, more spherical ice crystals. This leads to the largest crystals with the most extreme habits remaining (Fig. 6), allowing for the continued generation of aggregates (Fig. 5j, red) and hence snow (Fig. 3i, red) for AHM-AGG-IPAS. This shape effect on aggregation in AHM-AGG-IPAS allows not only for the hydrometeors to continue to lose mass based on crystal shape during sedimentation, rather than quickly once a threshold is met, but also allows for aggregates to continue to form (Fig. 5j, solid), which provides an additional source of snow mass to subsequently melt (Fig. 5j, dashed).

In addition to these low-level implications, enhancements in the averaged ice deposition/sublimation occur at 10-14 km for the AHM-AGG-IPAS scheme (Fig. 5h, red), exceeding AHM-ICE-ONLY and AHM-AGG-ORIG, yet the averaged ice mass of AHM-ICE-ONLY is vastly larger throughout the profile, including this upper-level section (Fig. 3h). The reason for these fea-



Accepted for publication in *Journal of the Atmospheric Sciences*. DOI 10.1175/JAS-D-20-0020.1.

tures is illustrated in Fig. 7, where the top row shows the process rates affecting ice in this area: growth due to deposition (IDEP, blue), loss due to sublimation (ISUB, green), and loss due to aggregation (IIAGG, red). The differences among the three (IDEP-ISUB-IIAGG, where all are positive values) are shown in Fig. 7, second row. Integration in Fig. 7 is over all points in the horizontal and at heights of 10-14 km. Note that the bars in Fig. 7 are *accumulating* (not stacking), meaning that the value of the bar corresponds to the bar height indicated by the y-axis. AHM-AGG-IPAS shows that total ice deposition in this region exceeds the rates in both AHM-ICE-ONLY and AHM-AGG-ORIG: the loss of ice to aggregation and subsequent sedimentation results in more available vapor over a lower ice mass. Similarly, the rates of sublimation and aggregation are significant as well. In fact, the integrated differences among these processes (row 2) illustrate that deposition rates always exceed sublimation in AHM-ICE-ONLY, whereas except at the beginning of the simulation, the combination of sublimation and aggregation in AHM-AGG-ORIG and AHM-AGG-IPAS result in a net loss of ice between 10-14 km. Hence, the introduction of aggregation (snow) not only results in an overall reduction of ice, it also appears to enhance ice processes aloft within the first 100 min of the simulation.

In addition to enhancements in ice deposition/sublimation, enhancements also appear for snow deposition/sublimation, cloud condensation, and cloud drop freezing between 10-14 km for the AHM-AGG-IPAS scheme (Figs. 5h,i,f,g, respectively). Investigation into these upper-level enhancements are explored in Fig. 8, where time series for all three AHM schemes (left: AHM-ICE-ONLY, middle: AHM-AGG-ORIG, right: AHM-AGG-IPAS) are shown for (row 1) integrated process rates affecting cloud droplets (negligible rates are excluded), (row 2) total number of grid boxes where relative humidity $\geq 100\%$ for liquid before and after a saturation adjustment and for (row 3) ice, and (row 4) total number of grid boxes where sublimation rates exceed deposition



Accepted for publication in *Journal of the Atmospheric Sciences*. DOI10.1175/JAS-D-20-0020.1.

rates for ice (blue), snow (orange), and ice+snow+graupel, exclusively[6] (green). As in Fig. 7, the bars in Fig. 8 are accumulating (not stacking), where the value of the bar corresponds to the bar height indicated by the y-axis.

Cloud condensation, as modeled in the AHM, cannot occur unless the environment is supersaturated with respect to liquid. The simulation average liquid saturation within 10-14 km is $\sim$20-50% (not shown); however, Fig. 8 shows cloud condensation occurring at relatively large rates in AHM-AGG-IPAS (right), reflecting the averaged enhancements in Fig. 5. Further, when integrating the domain grid points where relative humidity with respect to liquid exceeds 100% (Fig. 8, row 2, green), while some time steps indicate grid points meeting this threshold (0.5% at 70 mins), there are times where negligible points are saturated ($<$0.1%), and yet condensation occurs. However, note that 40-50% (Fig. 8, row 3) of the grid points achieve a supersaturation with respect to ice within this domain and at all times. Further investigation into the AHM parameterization reveals that, within one time step, the following calculations occur: calculation of relative humidity $\rightarrow$ ice/snow/graupel deposition/sublimation $\rightarrow$ saturation adjustment $\rightarrow$ cloud condensation/evaporation $\rightarrow$ homogeneous freezing. So, the environment is initially subsaturated, leading to sublimation of snow, ice, and graupel (Fig. 8, row 4). The order of the parameterization thus suggests that following these processes and the saturation adjustment, the environment experiences an increase in relative humidity (Fig. 8, row 2, purple) such that cloud condensation can occur. However, given that temperature within this vertical space is $\leq -40^{\circ}$C (Fig. 6, left), all newly condensed droplets freeze homogeneously thereafter (Fig. 8, top, blue – at-times hidden CFRZ bar tops indicated by blue asterisks). This process explains the reason for enhancements in cloud processes between 10-14 km (Fig. 5f,g), while no cloud water exists (Fig. 3f and Fig. 4a-c).

[6]"Exclusively" means that only the grid points where all three (ice, snow, and graupel) exist are counted, in contrast to "inclusively," which would mean that all grid points with ice alone + all grid points with snow alone + all grid points with graupel alone are counted, which is not the case here.



Accepted for publication in *Journal of the Atmospheric Sciences*. DOI10.1175/JAS-D-20-0020.1.

Note that these enhancements aloft (cloud condensation and subsequent freezing) are likely artifacts of the parameterization rather than realistic signatures. This is a result of the way (order) in which the microphysical processes are computed, and the subsequent saturation adjustments required for model stability. It is unphysical for ice/snow sublimation to result in supersaturation; however, this can occur as a byproduct of the parameterization methodology commonly implemented in bulk schemes, whereby process rates are computed based on the thermodynamics at the beginning of a timestep. This means that saturation can be overshot. Saturation adjustment, however, restricts this overshooting and thus maintains saturation in conjunction with subsequent homogeneous freezing. This sensitivity of the model to this parameterization methodology is noted, should be considered when interpreting results, and prompts a discussion on potential parameterization adjustments to consider. However, all parameterizations herein (M2M, THOM, and all AHM variations) compute condensation following all other processes and subsequent saturation adjustment, and so comparisons among the schemes remain valid.

In addition to the above, other unexpected signatures result from the inclusion of habit-dependent aggregation. The effect of the representation of snow on graupel formation is quite interesting. Graupel is enhanced for AHM-AGG-ORIG relative to AHM-ICE-ONLY, but decreases for AHM-AGG-IPAS (Fig. 2). Graupel time series (Fig. 3e) and vertical profiles (Fig. 3j) are similar for M2M and AHM-AGG-ORIG as well as for AHM-ICE-ONLY and AHM-AGG-IPAS. The formation of graupel in both AHM-ICE-ONLY and AHM-AGG-IPAS can only occur through ice-rain collection; because the way in which snow/aggregates are modeled differ between AHM-AGG-ORIG and AHM-AGG-IPAS, it is therefore not amenable to model riming of snow/aggregates in AHM-AGG-IPAS as in AHM-AGG-ORIG (following M2M). Hence, because AHM-AGG-ORIG is modeled after M2M and both AHM-ICE-ONLY and AHM-AGG-IPAS neglect the formation of graupel via riming of snow/aggregates, the patterns described above and in



Accepted for publication in *Journal of the Atmospheric Sciences*. DOI 10.1175/JAS-D-20-0020.1.

Fig. 3e,j make sense. This conclusion also implies that the magnitude of the gap in the two sets is due to riming of snow and cascading effects thereafter (e.g., further growth of graupel through deposition and collection). Enhanced graupel in AHM-AGG-ORIG also likely explains the slight drop in cloud mass mixing ratio relative to AHM-ICE-ONLY and AHM-AGG-IPAS between 0-100 min (Fig. 3a) and 6-10 km (Fig. 3f).

A further exploration of microphysical process rates for the three AHM schemes is presented in Fig. 9. Displayed are 36 rates that occur in one or more of the AHM schemes; rates not shown do not meet the lower bound of $10^{-8}$ or have negligible frequencies. Refer to Table 1 for process rates, including description and units for each rate. The x-axes indicate process rates binned by magnitude ($10^{-8}$ to $10^{2}$), and the color depth indicates the frequency of occurrence (total number of grid points) of that magnitude integrated over the entire domain and simulation time. Figures 9e-jj are process rates, or the transfer of mass due to a physical process, whereas the first four plots (Figs. 9a-d) are hydrometeor fluxes (sedimentation rates) and will be discussed in Sec. 4c.

The prior discussion on graupel formation is confirmed by the process rates in Fig. 9. Riming of cloud droplets (CSGRIME, Fig. 9hh) and rain (RSRIME, not shown) on snow occurs only for AHM-AGG-ORIG (middle row of each subplot). The processes reaching the highest magnitudes ($10^{1}$-$10^{2}$ g kg$^{-1}$ s$^{-1}$, although with relatively low frequencies) are self-collection of rain (NRAGG, Fig. 9y) and snow (NSAGG, Fig. 9z), which would affect rain and snow numbers, but not mass directly. In fact, the collection rate magnitudes are among the largest of all process rates, where rates within $10^{-1}$-$10^{0}$ g kg$^{-1}$ s$^{-1}$ are reached by the collection of cloud droplets by rain (CRACCR, Fig. 9q) and collection of ice by rain (IRRCOLL, Fig. 9ii). Following collection, the frequency of occurrence of growth by vapor deposition is significant, with rates occurring at multiple magnitudes. This appears for ice deposition/sublimation (IDEP/ISUB, Figs. 9g/k), snow deposition/sublimation (SDEP/SSUB, Figs. 9f/j), cloud droplet condensation/evaporation



Accepted for publication in *Journal of the Atmospheric Sciences*. DOI10.1175/JAS-D-20-0020.1.

(CCOND/CEVAP, Figs. 9e/i), and graupel deposition/evaporation (GDEP/GEVAP, Figs. 9h/l). Ice growth appears particularly significant, where snow growth rates increase for AHM-AGG-IPAS (bottom row of each subplot), as snow forms more readily via IPAS ice-ice aggregation (IIAGG, Fig. 9aa).

*b. Microphysical Sensitivity*

What is particularly interesting about Fig. 9 is the ability to gauge the general sensitivity of microphysical processes among the three schemes, or how the process of snow formation from ice affects other processes. There are a number of processes that have little or no sensitivity (negligible variation among the three schemes), such as cloud condensation/evaporation (CCOND/CEVAP, Fig. 9e/i), autoconversion of cloud to rain (CRAUTO, Fig. 9u), change in rain and ice masses due to ice-rain collisions (IRRCOLL, IRRSCOLL, and IRICOLL, Fig. 9ii, ee, and w), riming of droplets on graupel (CGRIME, Fig. 9ff), and melting and evaporation of graupel (GMELT and GEVAP, Fig. 9p and t). Most other processes show some variation in frequency or magnitude among the three schemes.

Further exploration into the relative sensitivity of each microphysical process among the three AHM schemes is presented in Fig. 10. The standard deviation of the three frequency values (for the three AHM schemes) is calculated for each binned magnitude from Fig. 9. The box and whisker plots thus show the spread in the frequency standard deviations for the 10 bins. Shown are the (a) actual and (b) mean-normalized spreads in the standard deviations (Fig. 10); the box encompasses the interquartile range (IQR); the whiskers encompass $\pm 1.5 \times$IQR; circles are outliers; also shown are data mean (green) and median (red). Interpretation of these results are as follows: (1) higher standard deviation values indicate larger differences, suggesting sensitivity, among the three schemes; (2) larger spread indicates not only differences among the schemes, but



Accepted for publication in *Journal of the Atmospheric Sciences*. DOI10.1175/JAS-D-20-0020.1.

that these differences vary across magnitudes (bins). The actual standard deviation (Fig. 10a) indicates the processes with not only the largest frequencies of occurrence within the domain, but also larger differences in frequencies among the three schemes; it is clear that the most significant processes, or those that contribute most to the mass flux, within the three AHM schemes are ice and snow sedimentation rates, deposition and sublimation, and aggregation. However, these results are weighted toward processes with higher magnitudes, and not indicative of the actual sensitivity of the processes. Hence, the standard deviations taken among the frequency values are normalized by the mean for the three schemes at each magnitude (within each bin) in Fig. 10b.

First, as discussed above, the processes with negligible sensitivity (i.e., CCOND, CEVAP, CRAUTO, IRRSCOLL, GEVAP, RGSPLINT,and CGRIME) have lower standard deviations ($<$ 0.2) and minimal spread; the processes in this category are mostly those affecting cloud droplets and graupel. Processes that have lower standard deviations yet show more spread are those with minor fluctuations in frequency but across many magnitudes (e.g., CRACCR, GMELT, CRACCR), suggesting a slight sensitivity to the selected scheme; the processes in this category are mostly those affecting cloud droplets, rain, and graupel. Increasing standard deviation values indicate increasing sensitivity (variation among schemes), and are mostly dominated by ice and snow processes, as would be expected. Finally, processes with larger spread and higher standard deviations are those where frequencies both fluctuate among schemes and across multiple magnitudes (bins), indicating that the sensitivity to the three schemes varies non-uniformly across rate magnitudes (e.g., CFRZ, SDEP, SSUB). Processes that occur in only one scheme have zero spread (i.e., SEVAP, CSSRIME, NSAGG, ISAUTO, CSGRIME, and RSRIME).

Figure 10 provides an overview of how each microphysical process responds to the physical variations among the three schemes and provides an indication of *relative* sensitivity. However, this illustration only provides the sensitivities of the processes relative to each other; it does not



Accepted for publication in *Journal of the Atmospheric Sciences*. DOI10.1175/JAS-D-20-0020.1.

indicate the significance of that sensitivity to the system as a whole. The scatter plot in Fig. 11 serves this purpose. The sum-total frequency values, or the frequency values of the three schemes added together across all bins for a process, indicating the total number of grid points in which that process occurs, is plotted with respect to the mean of the 10 mean-normalized standard deviations for a process (green lines, Fig. 10b). Circle size corresponds to the y-axis, or the significance of that process to the system, and circle color corresponds to the x-axis, or the sensitivity of that process to the scheme. Processes with zero spread are excluded.

The processes with the largest mean standard deviation (largest sensitivity), melting of snow (SMELT) and freezing of cloud droplets (CFRZ), also have some of the lowest frequency sums (lower significance). This means CFRZ and SMELT vary among the three schemes but that the number of grid points in which they occur is relatively low, which makes sense as snow only melts near the surface and cloud droplets homogeneously freeze aloft, and contribute little to the overall mass budget. Similarly, processes including freezing of rain (RFRZ) and nucleation (INUC) and melting of ice (IMELT) show moderate sensitivity ($0.2 < \sigma < 0.6$) to the three schemes, yet contribute less to the overall mass budget. A cluster of processes with relatively low sensitivity and significance (purple) appears, which, as discussed above, are cloud, rain, and graupel processes, and so would be considered relatively unaffected by the way in which aggregation is (or is not) simulated. Ice deposition (IDEP), sublimation (ISUB), and sedimentation (ISED) contribute to the system moderately to significantly, yet have relatively low sensitivity among the three schemes, although not negligible. Finally, as would be expected, ice-ice aggregation (IIAGG), and snow sublimation (SSUB), deposition (SDEP), and sedimentation (SSED) are sensitive to the three schemes, and are moderately significant in their contribution to the overall mass budget of the system.

In summary, clusters emerge that provide an overview of the significance of microphysical process rates and their sensitivity to changes in the way in which ice-ice aggregation (and cascading



Accepted for publication in *Journal of the Atmospheric Sciences*. DOI10.1175/JAS-D-20-0020.1.

processes) affect the mass budget of the system. Graupel, rain, and cloud processes have both significance and sensitivity that are low-moderate. Ice growth and sedimentation processes are significant, but low-moderately sensitive, whereas snow formation and sedimentation are highly sensitive and moderately significant. This illustration indicates that while some processes are very sensitive to these parameterization techniques, e.g., SMELT and CFRZ, their overall contribution to the system as a whole is less significant than other processes, but, that their consequences should not be discounted in future investigations. However, as would be expected, snow processes such as deposition/sublimation are sensitive to aggregation and significant in the simulation (and in fact are more sensitive than aggregation itself), and so inaccurate representation of aggregation can impact these processes and ultimately the phase partitioning within the system. Finally, note that the sedimentation rates of rain (RSED), graupel (GSED), ice (ISED), and snow (SSED) range from low to highly sensitive, yet, are all moderate to highly significant to the system mass budget, and are discussed further next.

*c. Precipitation Response*

The first four plots in Figs. 9 (a-d) and 10 show the sedimentation rates of rain and cloud droplets (RSED), snow (SSED), ice (ISED), and graupel (GSED). The highest frequencies occur at large magnitudes ($10^0$-$10^1$ g m$^{-2}$ s$^{-1}$, Fig. 9) for graupel, followed by rain, although a relatively small frequency of rain and smaller frequency of graupel fall in the highest magnitude range of $10^1$-$10^2$ g m$^{-2}$ s$^{-1}$. A larger frequency of snow occurs at a slightly lower magnitude ($10^{-1}$-$10^0$ g m$^{-2}$ s$^{-1}$) for AHM-AGG-ORIG (middle, Fig. 9b) and AHM-AGG-IPAS (bottom), where this flux is in the form of ice for AHM-ICE-ONLY (top, Fig. 9c). Interesting trends emerge in these four fluxes: the sedimentation frequency increases relatively uniformly with increasing magnitude for rain and graupel, which makes sense given their spherical nature. In contrast, ice sedimentation is more



Accepted for publication in *Journal of the Atmospheric Sciences*. DOI10.1175/JAS-D-20-0020.1.

frequent at lower magnitudes (indicating slower fall speeds), and snow sedimentation frequency pops between $10^{-1}$-$10^{1}$ g m$^{-2}$ s$^{-1}$.

Overall, the sedimentation rates of ice and snow have the largest differences among the three schemes (larger standard deviations) and at multiple rate magnitudes (larger spread, Fig. 10) relative to rain and graupel, with snow being the most sensitive (Fig. 11). Further, while ice sedimentation contributes most significantly to the total mass budget of the system (Fig. 7c), all hydrometeors contribute.

While all hydrometeors contribute to the total mass budget in the system, in this idealized case, ultimately the precipitation reaching the surface is in the form of rain given a surface temperature well above freezing (melting level $\sim$4 km). Figure 12 shows the (top) domain total precipitation every 10 min, as well as the (bottom) final total accumulated precipitation for each scheme for the duration of the simulation. THOM produces the most precipitation, peaking within the first third of the simulation and dropping significantly thereafter (Fig. 12, top, purple). This initial peak is reflected in the enhanced total accumulated precipitation signature. Meanwhile, precipitation amounts are relatively consistent among the remaining schemes, with M2M (blue) and AHM-AGG-IPAS (red) having similar quantities, and AHM-ICE-ONLY (gold) and AHM-AGG-ORIG (green) having the lowest values until the final 20 min. Further, it can be surmised that the growth by collection in AHM-AGG-ORIG (green) overtakes the growth by ice deposition in AHM-ICE-ONLY (gold) in terms of producing precipitable hydrometeors given their reversal in magnitudes midway through the simulation. Note that the addition of snow, which melts to rain (rather than sublimating aloft as ice in AHM-ICE-ONLY) increases the spatial distribution of surface precipitation for AHM-AGG-ORIG and AHM-AGG-IPAS as compared to AHM-ICE-ONLY (Fig. 12, bottom).



Accepted for publication in *Journal of the Atmospheric Sciences*. DOI 10.1175/JAS-D-20-0020.1.

*d. Polarimetric Signatures*

Surface precipitation can be further explored through analysis of simulated radar variables, which, in more realistic scenarios, serves to compare directly to observations. Plots of horizontal reflectivity (Fig. 13) for AHM-ICE-ONLY, AHM-AGG-ORIG, AHM-AGG-IPAS, and M2M are generated at simulation hour 3 using the offline forward operator of Ryzhkov et al. (2011), which takes into account hydrometeor shape and density (see Sulia and Kumjian 2017a, for details on use of the forward operator with the AHM). Note that the forward operator requires at least two-moment predictions for hydrometer quantities (i.e., mass and number for ice, snow, rain, and graupel); hence, because THOM is a single-moment scheme (with the exception of two-moment cloud ice), it is excluded in this analysis due to the inability to perform apples-to-apples comparisons. Subsequent plots are generated analogously to Xue et al. (2017) (their Fig. 3), who similarly simulate this idealized case, including plots for MC3E observations (their Fig. 3a1 and b1) of reflectivity for the KVNX NEXRAD radar (Fig. 1) at 12 UTC on May 20, 2011, and so the analysis to follow includes comparisons to that study. Note, however, that Xue et al. (2017) do not use the forward operator of Ryzhkov et al. (2011) to compute radar reflectivity, but rather an algorithm from Sarkadi et al. (2016).

First, note that the inclusion of aggregation, and hence snow, increases the spatial distribution of reflectivity, evident in both cross sections and surface views. AHM-AGG-ORIG and M2M exhibit similar signatures, as would be expected given their likeness in parameterization, particularly for snow. AHM-AGG-IPAS shows increased spatial distribution, yet with relatively low reflectivity values (5-20 dBz), which is a result of ice-ice aggregation occurring all the way to the surface (Fig. 9f, red solid). The lower reflectivity magnitude is a result of the inclusion of ice-ice aggregation only, without the ability for snow to continue to grow via collection thereafter,



Accepted for publication in *Journal of the Atmospheric Sciences*. DOI10.1175/JAS-D-20-0020.1.

which would increase particle size and therefore the backscattered reflectivity. Future work that will include ice-aggregate and aggregate-aggregate collection will likely remedy this reflectivity underestimate.

Observations of reflectivity (Xue et al. 2017, their Fig. 3) clearly indicate two maxima in both cross sections and surface plots of reflectivity, both reaching magnitudes of 40-55 dBZ. The AHM-AGG-ORIG and M2M schemes capture these maxima, albeit at lower magnitudes of 30-45 dBZ. The only scheme that captures the horizontal spread as seen in the observations (spanning $\sim$100-360 km) is AHM-AGG-IPAS, yet at lower reflectivity values. Again, this is likely attributed to ice-ice aggregates (snow) reaching the surface but with the inability to grow to larger sizes via continued collection. The fact that only snow in AHM-AGG-IPAS is able to reach the surface is likely due to the non-spherical nature of the particles, which reduces the rates of sublimation and melting, as discussed above.

Further investigation of the resulting impact of the selected scheme on radar signatures is presented in Fig. 14. Contoured frequency by altitude diagrams (CFADs) are shown for the horizontal reflectivity factor ($Z_{\mathrm{H}}$), where the top row (Figs. 14a-d) is the total $Z_{\mathrm{H}}$, whereas the bottom row (Figs. 14e-h) displays the contribution of each hydrometeor to the total $Z_{\mathrm{H}}$. All CFADs show a general pattern of increasing $Z_{\mathrm{H}}$ with decreasing altitude resulting from the growth of hydrometeors during sedimentation. The maximum reflectivity for all CFADs reaching nearly 40 dBZ within the lowest 2.5 km is attributed to rain (bottom row, green contours), whereas the secondary maximum reaching nearly 25-30 dBZ within 3-10 km is attributed to graupel (red contours). This is not surprising because the graupel and rain processes in all AHM simulations are modeled after the M2M parameterizations. The large frequency signature aloft in the AHM-AGG-IPAS (Fig. 14c) is attributed to the formation of snow/aggregates via ice-ice collection (Fig. 14g, grey). This signature is significant, and proceeds to relatively large values (reaching 20 dBZ) with decreasing altitude



Accepted for publication in *Journal of the Atmospheric Sciences*. DOI10.1175/JAS-D-20-0020.1.

all the way to the surface, which does not occur for any of the other schemes. This detection of snow accounts for the increased spatial distribution in surface reflectivity in Fig. 13.

It is interesting to note the differences in the contribution to $Z_{\mathrm{H}}$ from ice. The M2M scheme shows the contribution from ice at upper levels, whereas ice in all AHM simulations does not appear until around 10 km. However, Fig. 4k shows that the AHM-ICE-ONLY simulation produces the largest magnitude of ice throughout the domain compared to all other simulations, including at these higher altitudes. The lack of 'detection' of the plentiful ice in the forward operator aloft is due to the pristine nature of the crystals, where the density aloft in AHM-ICE-ONLY drops to as low as 200 kg $\mathrm{m}^{-3}$ (not shown). The returned backscattered power as simulated by the forward operator decreases with density, as it is a measure of the particle dielectric constant. This indicates the caution that must be taken when deriving mass or hydrometeor type from radar reflectivity.

Finally, the benefit of using the forward operator of Ryzhkov et al. (2011) with the AHM is the ability to generate dual-polarization quantities (see Sulia and Kumjian 2017a,b, for details), and this is the first time that snow habit and density are explicitly predicted by a bulk model and can be used to generate polarimetric variables, minimizing assumptions in calculations. Figure 15 includes (a-c) reflectivity $Z_{\mathrm{H}}$, (d-f) differential reflectivity $Z_{\mathrm{DR}}$, (g-i) specific differential phase $K_{\mathrm{DP}}$, (j-l) linear depolarization ratio $L_{\mathrm{DR}}$, and (m-o) correlation coefficient $\rho_{\mathrm{hv}}$ for AHM-ICE-ONLY, AHM-AGG-ORIG, and AHM-AGG-IPAS at the end of the simulation (hour 3). Note that M2M does not contain the shape or density information necessary to compute these quantities.

An increase in "detection" for all quantities appear for the AHM-AGG-IPAS scheme. Increased $Z_{\mathrm{H}}$ is indicative of larger backscattered power, which results from larger hydrometeors, or snow in this case. $Z_{\mathrm{DR}}$ is a bulk measurement of shape and orientation for all particles in a volume, $K_{\mathrm{DP}}$ is a bulk measurement of shape and orientation of only non-spherical particles in a volume, and $L_{\mathrm{DR}}$ is a measure of particle canting, enhanced by increasingly non-spherical particles. Hence,



Accepted for publication in *Journal of the Atmospheric Sciences*. DOI10.1175/JAS-D-20-0020.1.

all three are potential (depending on orientation) measures of non-spherical hydrometeors, and while ice is non-spherical in all three AHM schemes, snow aggregates are only non-spherical in AHM-AGG-IPAS. Since snow aggregates are larger than ice (Fig. 6), they are "detected" by the forward operator and so reflected in these signatures. Finally, $\rho_{\rm hv}$ is a measure of the diversity of the particles in a volume, and the contribution of snow hydrometeors in addition to rain and graupel (all of which are "detectable"), increases the particle diversity in both shape and density, decreasing the correlation coefficient.

Qualitative comparisons between Figs. 4 and 15 illustrate obvious similarities. First, note that the enhancement in $Z_{\rm H}$ from 0-5 km corresponds with the $q_r$ signature in all three schemes, with the highest reflectivities resulting from the largest $q_r$ quantities. No other hydrometeor mass appears in this region at these magnitudes. Similarly, the presence of graupel ($q_g$), which are simulated as spherical hydrometeors, are particularly evident in the AHM-AGG-IPAS case (Fig. 15, right) between x = 250$\sim$300 km and extending from 1$\sim$12 km in the vertical. The impact of $q_g$ on the bulk polarimetric signatures result in higher $Z_{\rm H}$ (up to 20 dBz) but obvious reductions in $L_{\rm DR}$ ($< -50$ dB), $Z_{\rm DR}$ (0 dB), and $K_{\rm DP}$. The values of $\rho_{\rm hv}$ near 1.0 indicate a lack of diversity, and likely the graupel are dominating this signature. Enhancements in $Z_{\rm H}$ accompanied by lack of all other polarimetric signatures for regions dominated by $q_r$ and $q_g$ follows what is expected for a deep convective storm (e.g., Ryzhkov and Zrnic 2019, their Fig. 9.10). In contrast, $q_i$ and $q_s$ dominate what would be expected as non-spherical polarimetric signatures (e.g., Kumjian 2013). Because there is no snow in AHM-ICE-ONLY, the signatures in Fig. 15 (left) are a result of non-spherical ice and match the $q_i$ cross section in Fig. 4k (i.e., $Z_{\rm DR} > 0$ dB, $K_{\rm DP} > 0$ °C km$^{-1}$, $L_{\rm DR} > -50$ dB, and $\rho_{\rm hv} < 1.0$). In contrast, while AHM-AGG-IPAS contains both non-spherical ice and snow, the size of snow will obfuscate detection of ice, and so these shape-dependent polarimetric signatures in Fig. 15 (right) are predominantly a reflection of the $q_s$ cross section in Fig. 4r. Note



Accepted for publication in *Journal of the Atmospheric Sciences*. DOI10.1175/JAS-D-20-0020.1.

the lack of significant shape-dependent polarimetric signature in AHM-AGG-ORIG. While this scheme contains non-spherical ice growth, it also contains snow, but simulated as low-density spheres, which, in addition to graupel (Fig. 4q) is a dominant hydrometeor (Fig. 4v). Hence, any non-spherical polarimetric signatures produced by ice will be obfuscated by snow and graupel in AHM-AGG-ORIG. Regardless, with the inclusion of habit-dependent snow generation via ice-ice aggregation, the polarimetric signatures begin to match what is typically expected (e.g., Kumjian 2013) for non-spherical detection of both ice and snow/aggregates.

## 5. Conclusions

The adaptive habit model (AHM, Harrington et al. 2013a) is an approach for more accurately representing the non-spherical growth of ice crystals in a bulk sense, capturing the nonlinear evolution in particle shape, size, and density. The complexity associated with the AHM parameterization requires careful development of processes subsequent to ice depositional growth, including riming and aggregation, among others. Jensen and Harrington (2015) introduce methodologies for the detailed representation of riming for the AHM (though not considered herein); however, detailed representation of aggregation is needed. Hence, this work introduces a novel approach to the representation of aggregation for the AHM, or for a microphysical scheme that considers non-spherical ice crystals with evolving aspect ratio and density.

Using both IPAS (Schmitt and Heymsfield 2010, 2014; Przybylo et al. 2019) for this purpose and the modified hydrodynamical collection kernel modified to account for non-spherical ice, a new scheme that considers ice particle shape and density for ice-ice aggregation has been implemented into the AHM. This scheme allows for not only the formation of aggregates from the existing non-spherical ice population, but includes the prediction of aggregation, or snow, characteristics, including shape and density. This is done using IPAS, which was specifically designed to return



Accepted for publication in *Journal of the Atmospheric Sciences*. DOI10.1175/JAS-D-20-0020.1.

the bulk characteristics necessary for AHM implementation. However, note that the amenability of IPAS permits that analogous methodologies could be developed for other commonly used microphysical models.

This methodology is tested for an idealized squall line based on the well-observed May 20, 2011, squall line from the MC3E field campaign following Xue et al. (2017) and Kacan and Lebo (2019). Simulations were performed for three microphysics schemes, Thompson et al. (2008) (THOM), Morrison et al. (2005) (M2M), and the AHM. Emphasis is placed on the AHM, where three variations are explored: (1) ice-only (AHM-ICE-ONLY), (2) ice and snow aggregates following M2M with modifications (AHM-AGG-ORIG), and (3) ice and snow aggregates using the new parameterization of this work (AHM-AGG-IPAS). Idealization is opted to explore the microphysical impacts of the new scheme without introducing more complex interactions. More realistic simulations will be considered in future work.

Microphysical analyses are explored, and many results are as expected. These include the reduction of ice mass relative to AHM-ICE-ONLY at the expense of snow (aggregates) following aggregation in all other schemes and AHM variations. The new AHM-AGG-IPAS scheme include some interesting cascading effects: (1) enhancements in process rates aloft (e.g., deposition/sublimation, condensation, homogeneous freezing) and (2) persistence of snow/aggregates well below the melting level due to continued ice-ice aggregation and persistent melting and sublimation of snow.

In addition to the impacts on subsequent processes, an investigation is performed to assess which processes are most sensitive to the way in which aggregation is parameterized in the AHM, and the significance of those processes. It is determined that as to be expected, snow-related processes, including deposition, sublimation, sedimentation, and formation via ice-ice aggregation, are all sensitive to this test, and moderately significant to the overall system mass budget. Further, ice processes are significant to the system, but less sensitive, though non-negligible, to these param-



Accepted for publication in *Journal of the Atmospheric Sciences*. DOI10.1175/JAS-D-20-0020.1.

eterizations. In contrast, processes such as homogeneous freezing, nucleation, and melting are moderate-highly sensitive to the aggregation schemes, but contribute little to the overall mass budget. Finally, remaining cloud, graupel, and rain processes vary in significance to the mass budget, but are generally insensitive to the new scheme. Regardless of sensitivity, sedimentation of all hydrometeors contributes significantly to the overall mass budget, as would be expected.

The new aggregation scheme results in the sedimentation of snow/aggregates to near the surface, unlike all other schemes. This is reflected in enhancements in surface precipitation for both rates and accumulation. These enhancements are captured in the simulated radar reflectively. The inclusion of aggregates/snow in any scheme should result in higher reflectivity values due to increased hydrometeor size, as well as the spatial expanse of reflectivity detected at the surface. AHM-AGG-IPAS underestimates reflectivity values at the surface (compared to Xue et al. 2017, their Fig. 3), and this is a result of the schemes aggregation limitation to ice-ice aggregation. It is anticipated that (ongoing) future work that considers subsequent collection of these particles will result in larger hydrometeor sizes and thus higher simulated reflectivities.

Finally, a benefit of the new aggregation scheme, like ice in the AHM, is the ability to predict and evolve aggregate shape and density. As a result, the polarimetric forward operator takes into account this information and can simulate dual-polarization quantities. This new AHM-AGG-IPAS scheme and the inclusion of this information results in a more realistic representation of polarimetric information. In fact, signatures appear in all quantities including reflectivity $Z_{\mathrm{H}}$, differential reflectivity $Z_{\mathrm{DR}}$, specific differential phase $K_{\mathrm{DP}}$, linear depolarization ratio $L_{\mathrm{DR}}$, and correlation coefficient $\rho_{\mathrm{hv}}$. These signatures are a result of not only the existence of snow/aggregates, which are more 'detectable' than ice given their size (AHM-AGG-ORIG), but also the shape information associated with these larger hydrometeors, which is revealed by the polarimetric quantities. The prediction of this information in models and the ability to translate to polarimetric radar variables



Accepted for publication in *Journal of the Atmospheric Sciences*. DOI10.1175/JAS-D-20-0020.1.

is particularly useful when comparing to and interpreting observations, the details of which will be explored in future work.

*Acknowledgments.* All authors would like to thank the Department of Energy for support under DOE Grant DE-SC0016354. K. Sulia is additionally supported through an appointment under the SUNY 2020 Initiative. The National Center for Atmospheric Research (C. Schmitt) is sponsored by the National Science Foundation. The authors would also like to extend their sincerest gratitude to the three anonymous reviewers who provided the necessary comments and discussion to help shape this work into its final form.



## References

Bergeron, T., 1935: On the physics of clouds and precipitation. Proces Verbaux de l'Association de Météorologie, International Union of Geodesy and Geophysics, 156–178.

Braham, R. R., Jr, 1968: Meteorological basis for precipitation development. *Bull. Amer. Meteor. Soc.*, **49 (4)**, 343–353.

Chen, J., and D. Lamb, 1994: The theoretical basis for the parameterization of ice crystal habits: Growth by vapor deposition. *J. Atmos. Sci.*, **51 (9)**, 1206–1221.

Connolly, P., C. Emersic, and P. Field, 2012: A laboratory investigation into the aggregation efficiency of ice crystals. *Atmos. Chem. and Phys.*, **12**, 2055–2076.

Findeisen, W., 1938: Kolloid-meteorologische Vorgänge bei Neiderschlags-bildung. Meteor. Z., **55**, 121–133.

Fukuta, N., and T. Takahashi, 1999: The growth of atmospheric ice crystals: A summary of findings in vertical supercooled cloud tunnel studies. *J. Atmos. Sci.*, **56**, 1963–1979.



Accepted for publication in *Journal of the Atmospheric Sciences*. DOI10.1175/JAS-D-20-0020.1.

Gaudet, L. C., K. J. Sulia, F. Yu, and G. Luo, 2019: Sensitivity of lake-effect cloud microphysical processes to ice crystal habit and nucleation during owles iop4. *J. Atmos. Sci.*, **76**, 3411–3434, doi:10.1175/JAS-D-19-0004.1.

Hall, W. D., 1980: A detailed microphysical model within a two-dimensional dynamic framework: Model description and preliminary results. *J. Atmos. Sci.*, **37**, 2486–2507.

Harrington, J., K. Sulia, and H. Morrison, 2013a: A method for adaptive habit prediction in bulk microphysical models. Part I: Theoretical development. *J. Atmos. Sci.*, **70**, 349–364, doi:10.1175/JAS-D-12-040.1.

Harrington, J., K. Sulia, and H. Morrison, 2013b: A method for adaptive habit prediction in bulk microphysical models. Part II: Parcel model corroboration. *J. Atmos. Sci.*, **70**, 365–376, doi:10.1175/JAS-D-12-0152.1.

Harrington, J. Y., A. Moyle, L. E. Hanson, and H. Morrison, 2019: On calculating deposition coefficients and aspect-ratio evolution in approximate models of ice crystal vapor growth. *J. Atmos. Sci.*, **76**, 1609–1625, doi:10.1175/JAS-D-18-0319.1.

Hashino, T., and G. Tripoli, 2008: The Spectral Ice Habit Prediction System (SHIPS). Part II: Simulation of nucleation and depositional growth polycrystals. *J. Atmos. Sci.*, **65**, 3071–3094, doi:10.1175/2008JAS2615.1.

Helmus, J. J., and S. M. Collis, 2016: The Python ARM Radar Toolkit (Py-ART), a Library for Working with Weather Radar Data in the Python Programming Language. *J. Open Res. Soft.*, **4 (1)**, doi:10.5334/JORS.119.



Accepted for publication in *Journal of the Atmospheric Sciences*. DOI10.1175/JAS-D-20-0020.1.

Heymsfield, A. J., C. Schmitt, and A. Bansemer, 2013: Ice cloud particle size distributions and pressure-dependent terminal velocities from in situ observations at temperatures from 0° to -86°c. *J. Atmos. Sci.*, **70**, 4123–4154, doi:10.1175/JAS-D-12-0124.1.

Hosler, C. L., D. C. Jensen, and L. Goldshlak, 1957: On the aggregation of ice crystals to form snow. *J. Meteor.*, **14**, 415–425.

Houghton, H. G., 1950: A preliminary quantitative analysis of precipitation mechanisms. *J. Meteor.*, **7**, 363–369.

Jensen, A., and J. Y. Harrington, 2015: Modeling ice crystal aspect ratio evolution during riming: A single particle growth model. *J. Atmos. Sci.*, **72**, 2569–2590, doi:10.1175/JAS-D-14-0297.1.

Jensen, A., J. Y. Harrington, and H. Morrison, 2018a: Impacts of ice particle shape and density evolution on the distribution of orographic precipitaiton. *J. Atmos. Sci.*, **75**, 3095–3114, doi:10.1175/JAS-D-17-0400.1.

Jensen, A., J. Y. Harrington, and H. Morrison, 2018b: Microphysical characteristics of sqall-line stratiform precipitation and transition zones simulated using an ice particle property-evolving model. *Mon. Wea. Rev.*, **146**, 723–743, doi:10.1175/MWR-D-17-0215.1.

Jensen, A., J. Y. Harrington, H. Morrison, and J. A. Milbrandt, 2017: Predicting ice shape evolution in a bulk microphysics model. *J. Atmos. Sci.*, **74**, 2081–2104, doi:10.1175/JAS-D-16-0350.1.

Jensen, M., and Coauthors, 2016: The Midlatitude Continental Convective Clouds Experiment (MC3E). *Bull. Amer. Meteor. Soc.*, **97 (9)**, 1667–1686, doi:10.1175/BAMS-D-14-00228.1.



Accepted for publication in *Journal of the Atmospheric Sciences*. DOI10.1175/JAS-D-20-0020.1.

Jiang, Z., M. Oue, J. Verlinde, E. E. Clothiaux, K. Aydin, and G. B. Y. Lu, 2017: What can we conclude about the real aspect ratios of ice particle aggregates from two-dimensional images? *J. Appl. Meteor. Climatol.*, **56**, 725–734.

Kacan, K. G., and Z. J. Lebo, 2019: Microphysical and Dynamical Effects of Mixed-Phase Hydrometeors in Convective Storms Using a Bin Microphysics Model: Melting. *Mon. Wea. Rev.*, **147 (12)**, 4437–4460, doi:10.1175/MWR-D-18-0032.1.

Key, J. R., P. Yang, B. A. Baum, and S. L. Nasiri, 2002: Parameterization of shortwave ice cloud optical properties for various particle habits. *J. Geophys. Res.*, **107 (D13)**, doi: 10.1029/2001JD000742.

Khain, A., A. Pokrovsky, M. Pinsky, A. Seifert, and V. Phillips, 1989: Simulation of effects of atmospheric aerosols on deep turbulent convective clouds using a spectral microphysics mixed-phase cumulus cloud model. Part I: Model description and possible applications. *J. Atmos. Sci.*, **61**, 2963–2982.

Koenig, L., 1971: Numerical modeling of ice deposition. *J. Atmos. Sci.*, **28**, 226–237.

Kumjian, M. R., 2013: Principles and applications of dual-polarization weather radar. Part I: Description of the polarimetric radar variables. *J. Operational Meteor.*, **1**, 226–242.

Kuroda, T., and R. Lacmann, 1982: Growth kinetics of ice from the vapor phase and its growth forms. *J. Crystal Growth*, **56**, 189–205.

Lin, Y., R. Farley, and H. Orville, 1983: Bulk parameterization of the snow field in a cloud model. *J. Climate Appl. Meteor.*, **22**, 1065–1092.

Morrison, H., G. de Boer, G. Feingold, J. Harrington, M. Shupe, and K. Sulia, 2012: Resilience of persistent Arctic mixed-phase clouds. *Nature Geosci.*, **5**, 11–17.



Accepted for publication in *Journal of the Atmospheric Sciences*. DOI10.1175/JAS-D-20-0020.1.

Morrison, H., and W. Grabowski, 2007: Comparison of bulk and bin warm rain microphysics models using a kinematic framework. *J. Atmos. Sci.*, **64**, 2839–2861.

Morrison, H., and W. Grabowski, 2010: An improved representation of rimed snow and conversion to graupel in a multicomponent bin microphysics scheme. *J. Atmos. Sci.*, **67**, 1337–1360, doi: 10.1175/2010JAS3250.1.

Morrison, H., and J. A. Milbrandt, 2015: Parameterization of cloud microphysics based on the prediction of bulk ice particle properties. Part I: Scheme description and idealized tests. *J. Atmos. Sci.*, **72**, 287–311, doi:10.1175/JAS-D-14-0065.1.

Morrison, H., M. Shupe, J. Pinto, and J. Curry, 2005: Possible roles of ice nucleation mode and ice nuclei depletion in the extended lifetime of Arctic mixed-phase clouds. *Geophys. Res. Let.*, **32**, L18 801, doi:10.1029/2005GL023614.

Morrison, H., G. Thompson, and V. Tatarskii, 2009: Impact of cloud microphysics on the development of trailing stratiform precipitation in a simulated squall line: Comparison of one- and two-moment schemes. *Mon. Wea. Rev.*, **137**, 991–1007, doi:10.1175/2008MWR2556.1.

Ono, A., 1969: The shape and riming properties of ice crystals in natural clouds. *J. Atmos. Sci.*, **26**, 138–147.

Ovchinnikov, M., and Coauthors, 2014: Intercomparison of large-eddy simulations of Arctic mixed-phase clouds: Importance of ice size distribution assumptions. *J. Advances Modeling Earth Sys.*, **6**, doi:10.1002/2013MS000282.

Passarelli, R. E., 1978: An approximate analytical model of the vapor deposition and aggregation of snowflakes. *J. Atmos. Sci.*, **35**, 118–124.



Accepted for publication in *Journal of the Atmospheric Sciences*. DOI10.1175/JAS-D-20-0020.1.

Phillips, V. T. J., M. Formenton, A. Bansemer, I. Kudzotsa, and B. Lienert, 2015: A parameterization of sticking efficiency for collisions of snow and graupel with ice crystals: theory and comparison with observations. *J. Atmos. Sci.*, **72 (6)**, 4885–4902.

Phillips, V. T. J., A. Pokrovsky, and A. Khain, 2007: The influence of time-dependent melting on the dynamics and precipitation production in maritime and continental storm clouds. *J. Atmos. Sci.*, **64**, 338–359.

Pruppacher, H. R., and J. D. Klett, 1997: *Microphysics of Clouds and Precipitation*. 2nd ed., Springer, 954 pp.

Przybylo, V. M., K. J. Sulia, C. G. Schmitt, Z. J. Lebo, and W. C. May, 2019: The ice particle and aggregate simulator (ipas). part i: Extracting dimensional properties of ice–ice aggregates for microphysical parameterization. *J. Atmos. Sci.*, **76**, 1661–1676, doi:10.1175/JAS-D-18-0187.1.

Reisner, J., R. Rasmussen, and R. Bruintjes, 1998: Explicit forecasting of supercooled liquid water in winter storms using the MM5 mesoscale model. *Quart. J. Roy. Meteor. Soc.*, **124**, 1071–1107.

Rogers, R. R., and M. K. Yau, 1989: A short course in cloud physics. Pergamon Press, chap. 12, 206.

Ryzhkov, A. V., M. Pinsky, A. Pokrovsky, and A. Khain, 2011: Polarimetric radar observation operator for a cloud model with spectral microphysics. *J. Appl. Meteor. Climatol.*, **50**, 873–894.

Ryzhkov, A. V., and D. S. Zrnic, 2019: *Radar Polarimetry for Weather Observations*. 1st ed., Springer, 486 pp.

Sarkadi, N., I. Geresdi, and G. Thompson, 2016: Numerical simulation of precipitation formation in the case orographically induced convective cloud: Comparison of the results of bin and bulk microphysical schemes. *Atmos. Res.*, **180**, 241–261, doi:10.1016/j.atmosres.2016.04.010.



Accepted for publication in *Journal of the Atmospheric Sciences*. DOI10.1175/JAS-D-20-0020.1.

Schmitt, C. G., and A. J. Heymsfield, 2010: The dimensional characteristics of ice crystal aggregates from fractal geometry. *J. Atmos. Sci.*, 1605–1616.

Schmitt, C. G., and A. J. Heymsfield, 2014: Observational quantification of the separation of simple and complex atmospheric ice particles. *Geophys. Res. Lett.*, 1301–1307.

Sulia, K., and J. Harrington, 2011: Ice aspect ratio influences on mixed-phase clouds: Impacts on phase partitioning in parcel models. *J. Geophys. Res.*, **116**.

Sulia, K. J., J. Y. Harrington, and H. Morrison, 2013: A method for adaptive habit prediction in bulk microphysical models. Part III: Applications and studies within a two-dimensional kinematic model. *J. Atmos. Sci.*, **70**, 3302–3320, doi:10.1175/JAS-D-12-0316.1.

Sulia, K. J., and M. R. Kumjian, 2017a: Simulated polarimetric fields using the adaptive habit model. Part I: LES. *Mon. Wea. Rev.*, **145 (6)**, 2281–2302, doi:10.1175/MWR-D-16-0061.1.

Sulia, K. J., and M. R. Kumjian, 2017b: Simulated polarimetric fields using the adaptive habit model. Part II: A case study from the FROST experiment. *Mon. Wea. Rev.*, **145 (6)**, 2303–2323, doi:10.1175/MWR-D-16-0061.1.

Sulia, K. J., H. Morrison, and J. Harrington, 2014: Dynamical and microphysical evolution during mixed-phase cloud glaciation simulated using the bulk adaptive habit prediction model. *J. Atmos. Sci.*, **71**, 4158–4180, doi:10.1175/JAS-D-14-0070.1.

Takano, Y., and K.-N. Liou, 1989: Solar radiative transfer in cirrus clouds. Part I: Single-scattering and optical properties of hexagonal ice crystals. *J. Atmos. Sci.*, **46 (1)**, 3–19.

Thompson, G., P. Field, R. Rasmussen, and W. Hall, 2008: Explicit forecasts of winter precipitation using an improved bulk microphysics scheme. Part II: Implementation of a new snow parameterization. *Mon. Wea. Rev.*, **136**, 5095–5115.



Accepted for publication in *Journal of the Atmospheric Sciences*. DOI10.1175/JAS-D-20-0020.1.

Thompson, G., R. Rasmussen, and K. Manning, 2004: Explicit forecasts of winter precipitation using an improved bulk microphysics scheme. Part I: Description and sensitivity analysis. *Mon. Wea. Rev.*, **132**, 519–542.

Walko, R., W. Cotton, M. Meyers, and J. Harrington, 1995: New RAMS cloud microphysics parameterization. Part I: The single-moment scheme. *Atmos. Res.*, **38**, 29–62.

Wegener, A., 1911: Thermodynamik der Atmosphäre, 331.

Woods, C., M. Stoelinga, and J. Locatelli, 2007: The IMPROVE-1 storm of 1-2 February 2001. Part III: Sensitivity of a mesoscale model simulation to the representation of snow particle types and testing of a bulk microphysical scheme with snow habit prediction. *J. Atmos. Sci.*, **64**, 3927–3948.

Xue, L., and Coauthors, 2017: Idealized Simulations of a Squall Line from the MC3E Field Campaign Applying Three Bin Microphysics Schemes: Dynamic and Thermodynamic Structure. *Mon. Wea. Rev.*, **145**, 4789–4812.





Accepted for publication in *Journal of the Atmospheric Sciences*. DOI 10.1175/JAS-D-20-0020.1.

## LIST OF TABLES







Accepted for publication in *Journal of the Atmospheric Sciences*. DOI 10.1175/JAS-D-20-0020.1.

| PROCESS | DESCRIPTION | UNITS |
|---|---|---|
| RSED | rain sedimentation rate | $g\ m^{-2}\ s^{-1}$ |
| SSED | snow sedimentation rate | $g\ m^{-2}\ s^{-1}$ |
| ISED | ice sedimentation rate | $g\ m^{-2}\ s^{-1}$ |
| GSED | graupel sedimentation rate | $g\ m^{-2}\ s^{-1}$ |
| NRAGG | rain self-collection | $\#\ kg^{-1}\ s^{-1} \times 10^{-3}$ |
| NSAGG | snow self-aggregation | $\#\ kg^{-1}\ s^{-1} \times 10^{-3}$ |
| IIAGG | ice-ice aggregation | $g\ kg^{-1}\ s^{-1}$ |
| CRACCR | accretion cloud droplets by rain | $g\ kg^{-1}\ s^{-1}$ |
| CRAUTO | autoconversion cloud droplets to rain | $g\ kg^{-1}\ s^{-1}$ |
| ISAUTO | autoconversion ice to snow | $g\ kg^{-1}\ s^{-1}$ |
| IRRCOLL | change in rain mass due to ice-rain collection, added to graupel | $g\ kg^{-1}\ s^{-1}$ |
| IRICOLL | change in ice mass due to ice-rain collection, added to graupel | $g\ kg^{-1}\ s^{-1}$ |
| IRRSCOLL | change in rain mass due to ice-rain collision, added to snow | $g\ kg^{-1}\ s^{-1}$ |
| IRSCOLL | change in snow mass due to ice-rain collision, added to snow | $g\ kg^{-1}\ s^{-1}$ |
| CGRIME | riming of cloud droplets on graupel | $g\ kg^{-1}\ s^{-1}$ |
| CSSRIME | riming cloud droplets on snow, added to snow | $g\ kg^{-1}\ s^{-1}$ |
| CSGRIME | riming of cloud droplets on snow, added to graupel | $g\ kg^{-1}\ s^{-1}$ |
| RSRIME | riming of rain on snow | $g\ kg^{-1}\ s^{-1}$ |
| GDEP | graupel deposition | $g\ kg^{-1}\ s^{-1}$ |
| GSUB | graupel sublimation | $g\ kg^{-1}\ s^{-1}$ |
| GEVAP | melting then evaporation of graupel | $g\ kg^{-1}\ s^{-1}$ |
| GMELT | graupel melting | $g\ kg^{-1}\ s^{-1}$ |
| CGSPLINT | splintering cloud droplets accreted onto graupel | $g\ kg^{-1}\ s^{-1}$ |
| RGSPLINT | splintering rain accreted onto graupel | $g\ kg^{-1}\ s^{-1}$ |
| SMELT | snow melting | $g\ kg^{-1}\ s^{-1}$ |
| IMELT | ice melting | $g\ kg^{-1}\ s^{-1}$ |
| IDEP | ice depositon | $g\ kg^{-1}\ s^{-1}$ |
| ISUB | ice sublimation | $g\ kg^{-1}\ s^{-1}$ |
| REVAP | rain evaporation | $g\ kg^{-1}\ s^{-1}$ |
| SEVAP | melting then evaporation of snow | $g\ kg^{-1}\ s^{-1}$ |
| SDEP | snow deposition | $g\ kg^{-1}\ s^{-1}$ |
| SSUB | snow sublimation | $g\ kg^{-1}\ s^{-1}$ |
| CCOND | cloud droplet condensation | $g\ kg^{-1}\ s^{-1}$ |
| CEVAP | cloud droplet evaporation | $g\ kg^{-1}\ s^{-1}$ |
| INUC | ice nucleation | $g\ kg^{-1}\ s^{-1}$ |
| RFRZ | freezing of rain | $g\ kg^{-1}\ s^{-1}$ |
| CFRZ | freezing of cloud droplets | $g\ kg^{-1}\ s^{-1}$ |

TABLE 1. Processes that are modeled in one or more of the simulations discussed herein. All quantities are mass mixing ratio or mass flux, except NRAGG and NSAGG, which are changes in number mixing ratio, as indicated by the units.



Accepted for publication in *Journal of the Atmospheric Sciences*. DOI10.1175/JAS-D-20-0020.1.

## LIST OF FIGURES





Accepted for publication in *Journal of the Atmospheric Sciences*. DOI10.1175/JAS-D-20-0020.1.

Accepted for publication in *Journal of the Atmospheric Sciences*. DOI10.1175/JAS-D-20-0020.1.

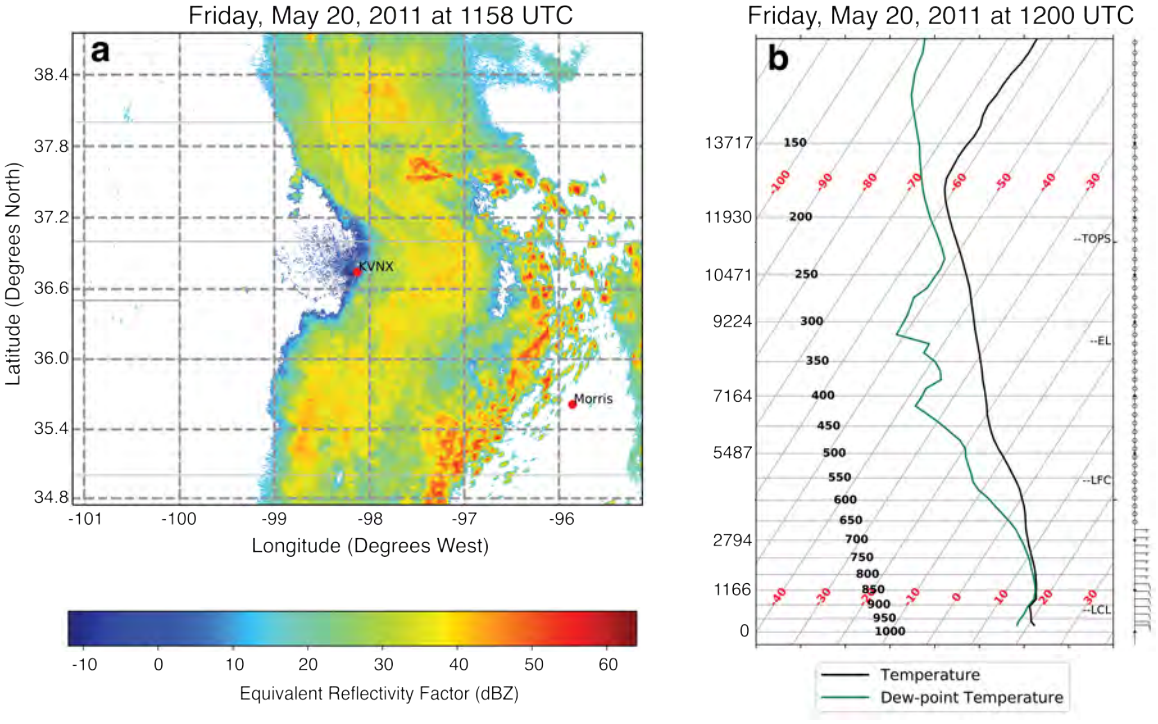


FIG. 1. (a) NEXRAD equivalent reflectivity factor at 1158 UTC 20 May 2011 for the KVNX radar in Vance AFB, Oklahoma as generated via Py-ART (Helmus and Collis 2016). Also indicated is the location in Morris, Oklahoma of the (b) sounding used to initialize this idealized case.





Accepted for publication in *Journal of the Atmospheric Sciences*. DOI 10.1175/JAS-D-20-0020.1.

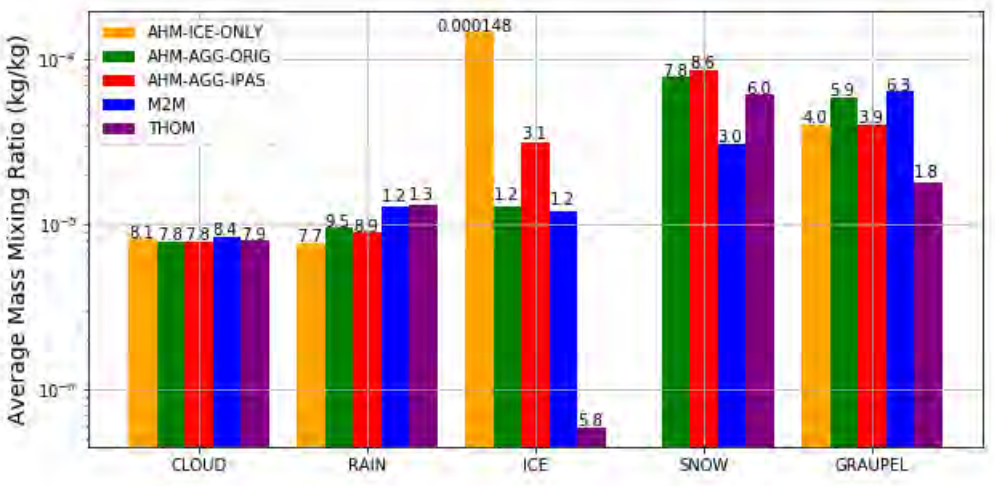


FIG. 2. Simulation-averaged (time and domain) hydrometeor mass mixing ratios (kg/kg) for AHM-ICE-ONLY (gold), AHM-AGG-ORIG (green), AHM-AGG-IPAS (red), M2M (blue), and THOM (purple). Values atop bars correspond to approximate average mass mixing ratios within the order of magnitude indicated (e.g., M2M average cloud mass mixing ratio $\approx 8.4 \times 10^{-6}$ kg/kg)

.



Accepted for publication in *Journal of the Atmospheric Sciences*. DOI 10.1175/JAS-D-20-0020.1.

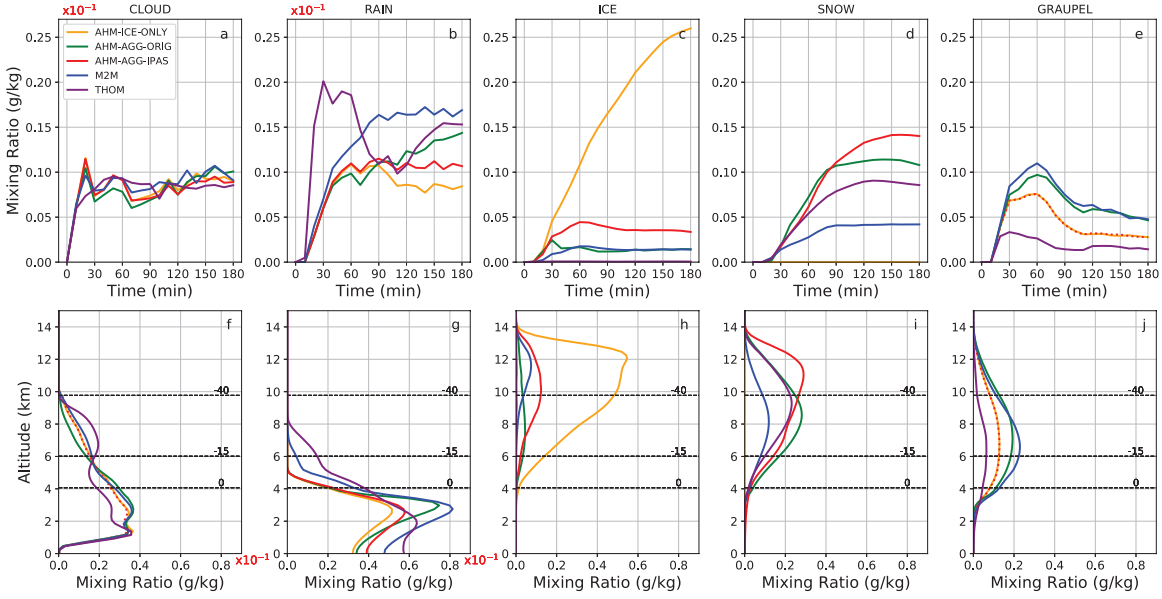


FIG. 3. (a-e) Time series of spatially averaged mixing ratios and (f-j) vertical profiles of horizontally and temporally averaged mixing ratios for (a,f) cloud droplets, (b,g) rain, (c,h) ice, (d,i) snow, and (e,j) graupel for each scheme: AHM-ICE-ONLY (gold), AHM-AGG-ORIG (green), AHM-AGG-IPAS (red), M2M (blue), and THOM (purple). Note that (a,f) cloud and (b,g) rain mixing ratios are one order of magnitude less than ice, snow, and graupel. Also note that AHM-AGG-IPAS lines (red) in e, f, and j are dotted only to distinguish from AHM-ICE-ONLY (gold). Dashed black horizontal lines (f-j) are the -40, -15, and 0°C isotherms.





Accepted for publication in *Journal of the Atmospheric Sciences*. DOI 10.1175/JAS-D-20-0020.1.

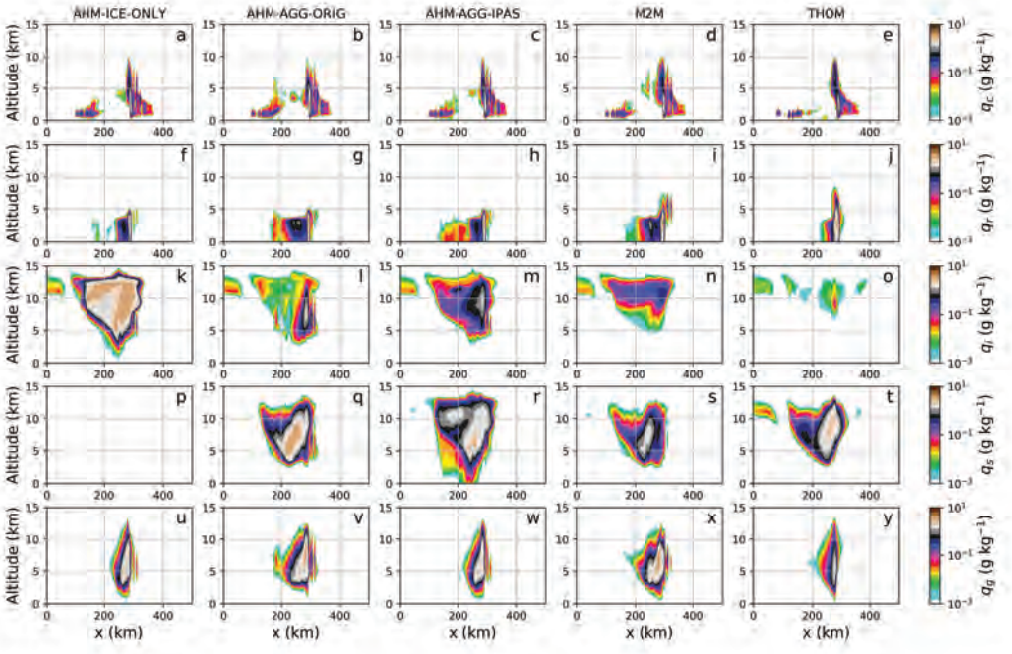


FIG. 4. Cross sections of (top to bottom) cloud, rain, ice, snow, and graupel mixing ratios averaged in the y-direction after 3 hr of simulation time for (left to right) AHM-ICE-ONLY, AHM-AGG-ORIG, AHM-AGG-IPAS, M2M, and THOM schemes.





Accepted for publication in *Journal of the Atmospheric Sciences*. DOI 10.1175/JAS-D-20-0020.1.

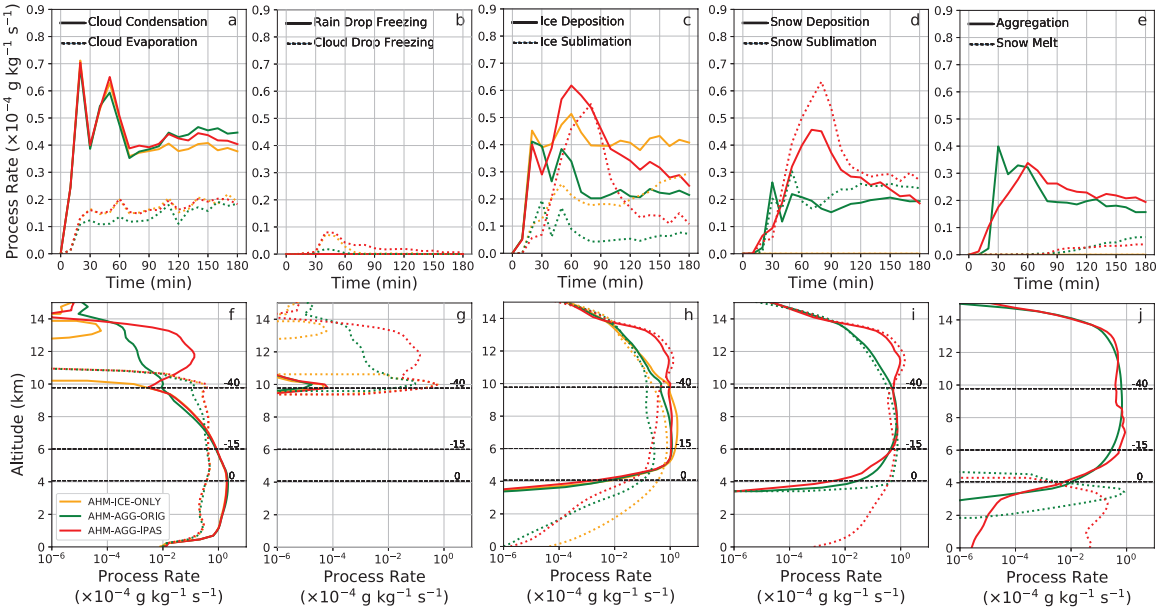


FIG. 5. (a-e) Time series of spatially averaged process rates and (f-j) vertical profiles of horizontally and temporally averaged process rates (note log scale) for (a,f) cloud droplet condensation (solid) and evaporation (dashed), (b,g) rain (solid) and cloud (dashed) droplet freezing, (c,h) ice deposition (solid) and sublimation (dashed), (d,i) snow deposition (solid) and sublimation (dashed), and (e,j) aggregation (solid) and melting snow (dashed) for AHM-ICE-ONLY (gold), AHM-AGG-ORIG (green), and AHM-AGG-IPAS (red). Dashed black lines (f-j) are the -40, -15, and 0°C isotherms.





Accepted for publication in *Journal of the Atmospheric Sciences*. DOI 10.1175/JAS-D-20-0020.1.

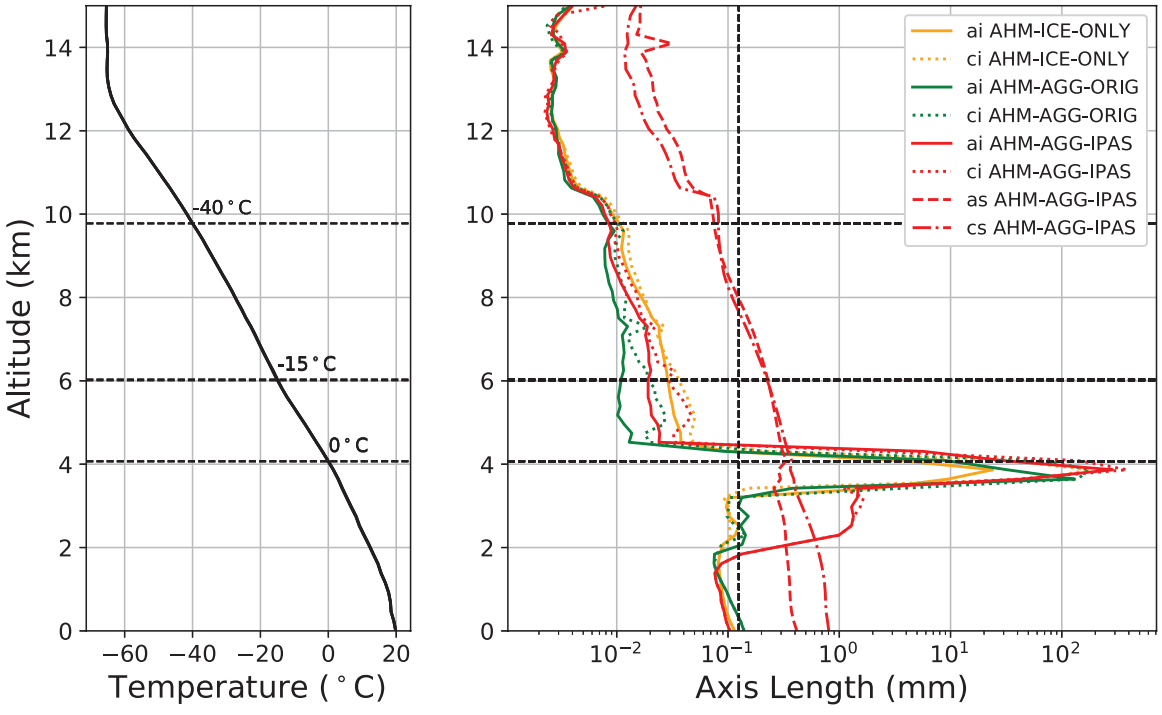


FIG. 6. (left) Vertical profiles of horizontally and temporally averaged temperature and (right) axis lengths for AHM-ICE-ONLY (gold), AHM-AGG-ORIG (green), and AHM-AGG-IPAS (red) schemes. All three schemes include ice *a* (solid) and *c* (dotted) axes, whereas AHM-AGG-IPAS also includes snow *a* (dashed) and *c* (dashed-dotted) axes. Dashed horizontal black lines on both plots are 0, -15, and -14°C isotherms, and the dashed vertical black line (right) is the 125 $\mu$m ice-snow autoconversion threshold for reference.





Accepted for publication in *Journal of the Atmospheric Sciences*. DOI 10.1175/JAS-D-20-0020.1.

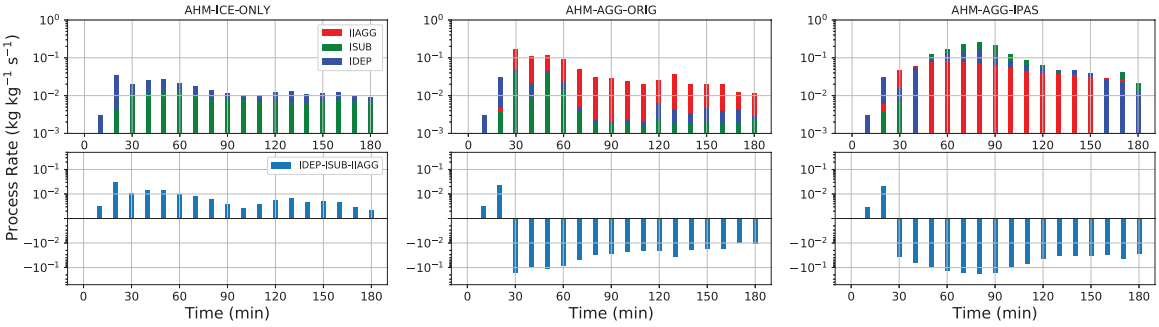


FIG. 7. **row 1:** Integrated process rates with respect to time affecting ice, including aggregation (IIAGG, red), sublimation (ISUB, green), and deposition (IDEP, blue). **row 2:** Integrated differences in process rates (i.e., IDEP-ISUB-IIAGG). Results for AHM-ICE-ONLY (left), AHM-AGG-ORIG (middle), and AHM-AGG-IPAS (right) are shown. Bars are accumulating (not stacking). Integration (for all plots) is performed over all horizontal grid points, but constrained to 10-14 km in the vertical. Negligible processes are excluded.





Accepted for publication in *Journal of the Atmospheric Sciences*. DOI 10.1175/JAS-D-20-0020.1.

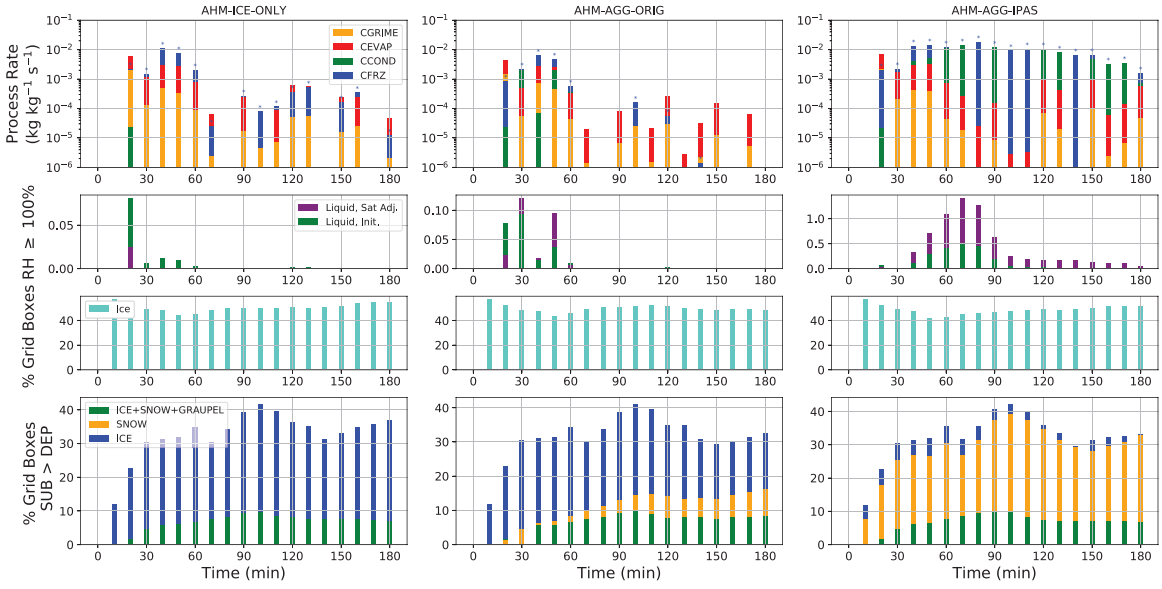


FIG. 8. **row 1:** Integrated process rates with respect to time affecting cloud droplets, including collection of cloud droplets on graupel (CGRIME, gold), cloud evaporation (CEVAP, red), cloud condensation (CCOND, green), and cloud droplet freezing (CFRZ, blue). The blue asterisks indicate the at-times hidden CFRZ bar top. **row 2:** Total number of grid points where relative humidity is $\geq 100\%$ for liquid before (green) and after (purple) a saturation adjustment. **row 3:** Total number of grid points where relative humidity is $\geq 100\%$ for ice. **row 4:** Total number of grid points where sublimation rates exceed deposition rates for ice (blue), snow (gold), and ice+snow+graupel, exclusively (green). Results for AHM-ICE-ONLY (left), AHM-AGG-ORIG (middle) and AHM-AGG-IPAS (right) are shown. Bars are accumulating (not stacking). Integration (for all plots) is performed over all horizontal grid points, but constrained to 10-14 km in the vertical. Negligible processes are excluded.





Accepted for publication in *Journal of the Atmospheric Sciences*. DOI 10.1175/JAS-D-20-0020.1.

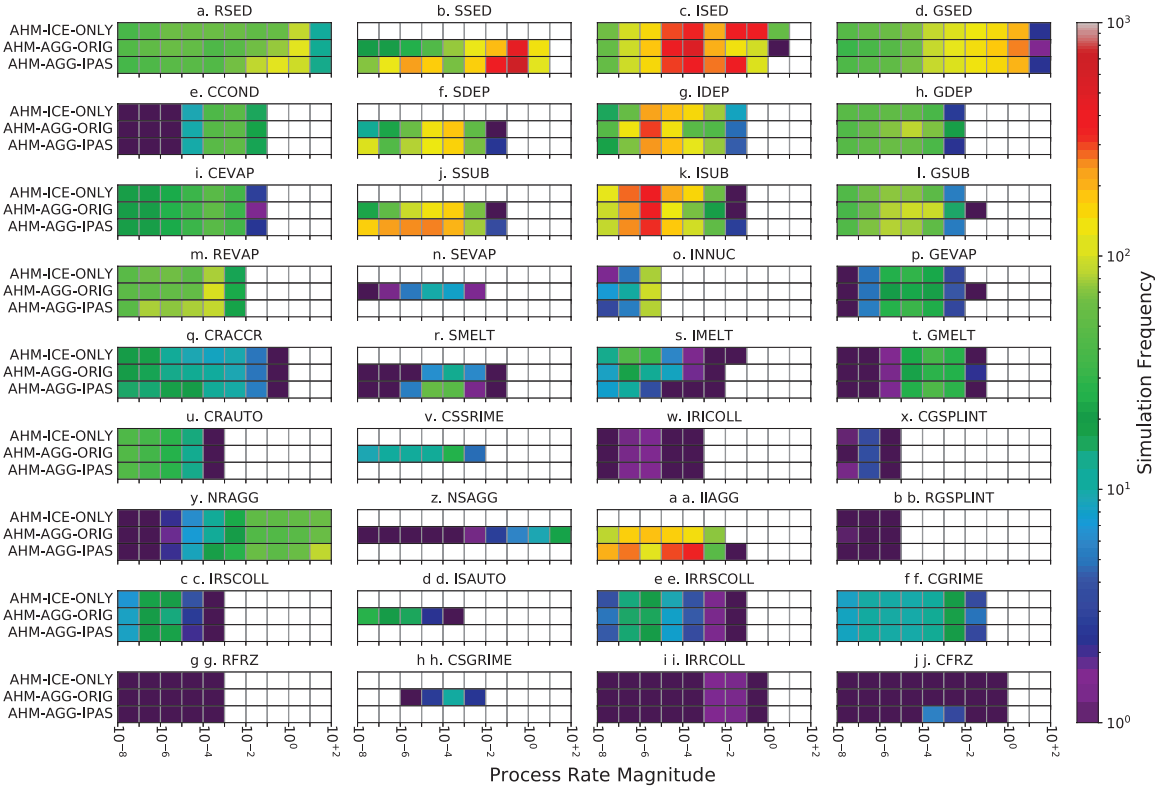


FIG. 9. Process rates, where the x-axis indicates the magnitude of the process rate (see Table 1 for units and description). All rates are binned in their respective order of magnitude ranging from $10^{-8}$ to $10^{2}$. The colormap indicates the simulation (domain and time) total frequency per magnitude (total number of grid points in space and time falling into each respective bin). Three schemes are included: AHM-ICE-ONLY (top row of each subplot), AHM-AGG-ORIG (middle row of each subplot), AHM-AGG-IPAS (bottom row of each subplot).





Accepted for publication in *Journal of the Atmospheric Sciences*. DOI 10.1175/JAS-D-20-0020.1.

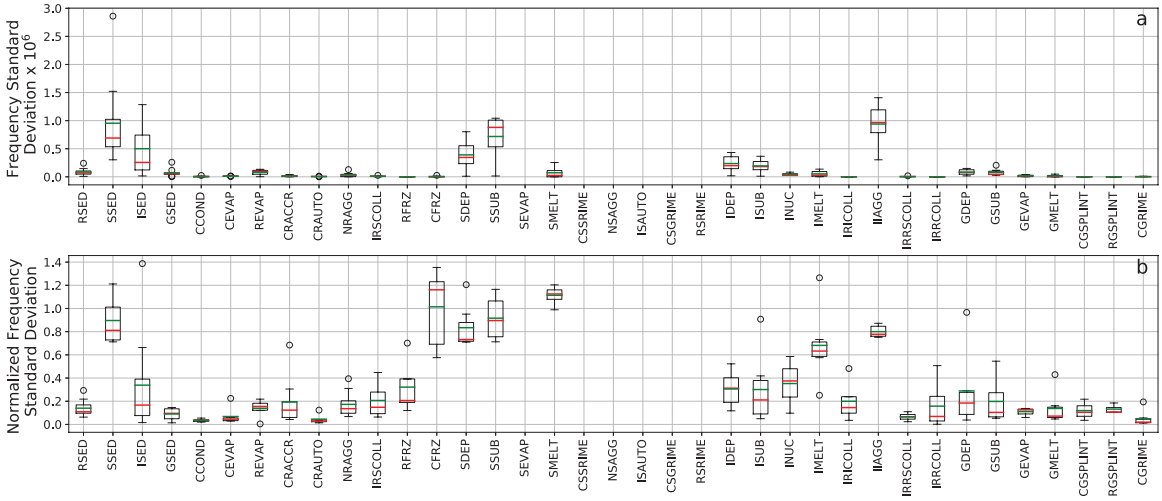


FIG. 10. Standard deviations are computed for the three frequency values among AHM-ICE-ONLY, AHM-AGG-ORIG, and AHM-AGG-IPAS within each binned magnitude range from Fig. 9. Shown here are box and whisker plots, indicating the spread in the (a) actual and (b) mean-normalized standard deviation of magnitude frequencies. The box extends to encompass the interquartile range (IQR), and the whiskers are $\pm 1.5 \times$IQR. Circles are outliers. Red lines are median; green lines are mean.



Accepted for publication in *Journal of the Atmospheric Sciences*. DOI 10.1175/JAS-D-20-0020.1.

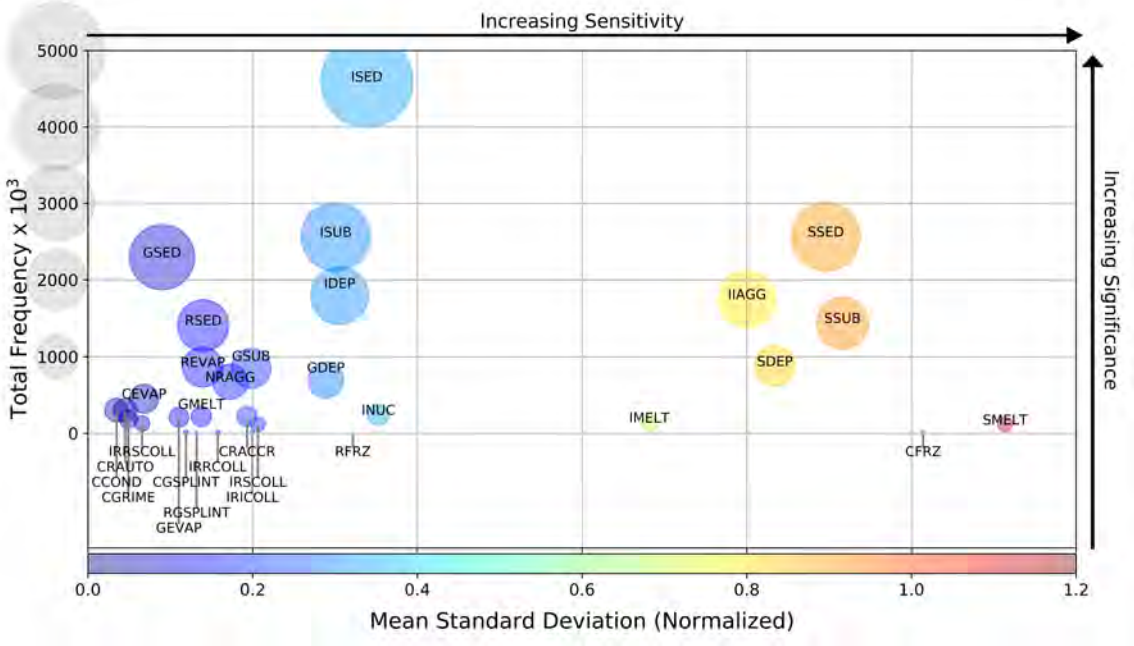


FIG. 11. Scatter plot indicating mean-normalized standard deviation (green lines in Fig. 10) of magnitude frequencies from Fig. 9 averaged over AHM-ICE-ONLY, AHM-AGG-ORIG, and AHM-AGG-IPAS with respect to total frequency. Circle size corresponds to the y-axis, and circle color corresponds to the x-axis. Processes with zero spread are excluded.



Accepted for publication in *Journal of the Atmospheric Sciences*. DOI 10.1175/JAS-D-20-0020.1.

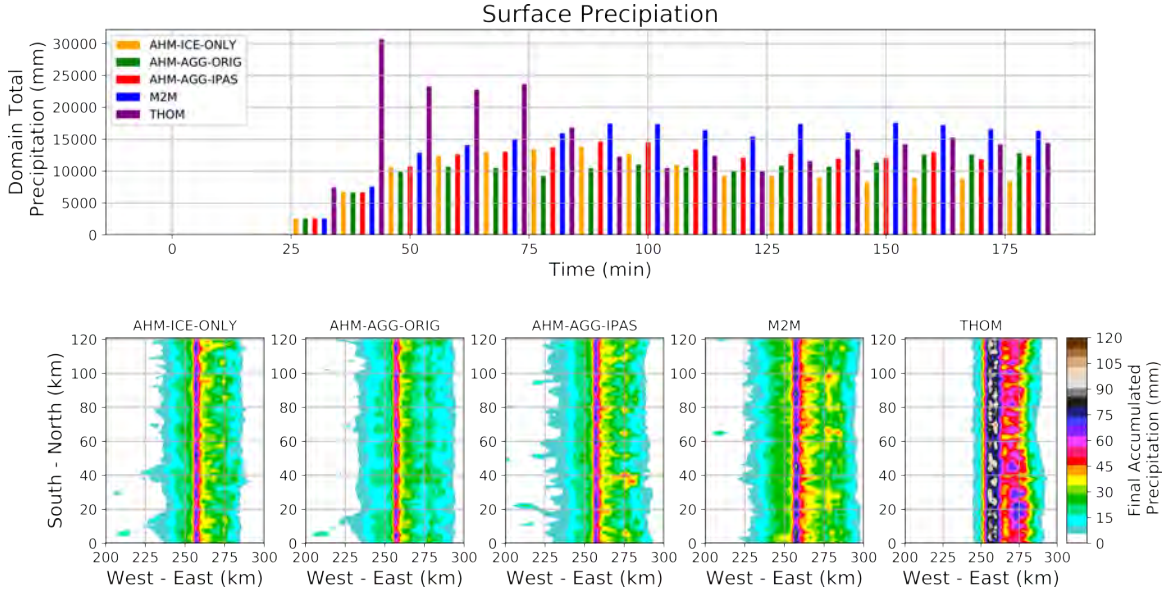


FIG. 12. (top) Time series of domain total precipitation (mm) and (bottom) final accumulated surface precipitation at 3 hr for AHM-ICE-ONLY, AHM-AGG-ORIG, AHM-AGG-IPAS, M2M, and THOM.





Accepted for publication in *Journal of the Atmospheric Sciences*. DOI 10.1175/JAS-D-20-0020.1.

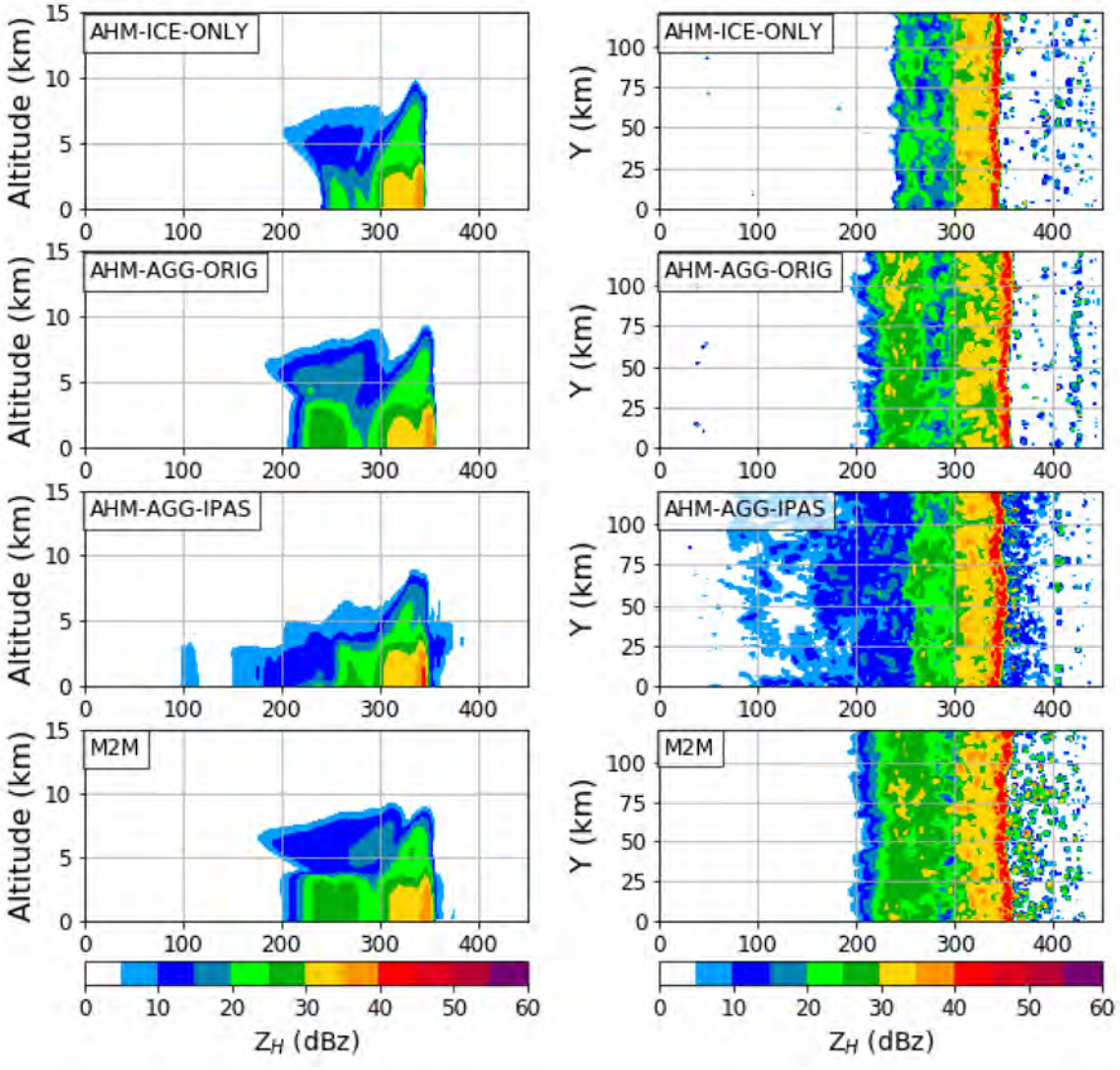


FIG. 13. Cross sections (averaged in the y-direction) and surface plots of reflectivity ($Z_H$) for AHM-ICE-ONLY, AHM-AGG-ORIG, AHM-AGG-IPAS, and M2M for comparisons to Fig. 3 in Xue et al. (2017)





Accepted for publication in *Journal of the Atmospheric Sciences*. DOI 10.1175/JAS-D-20-0020.1.

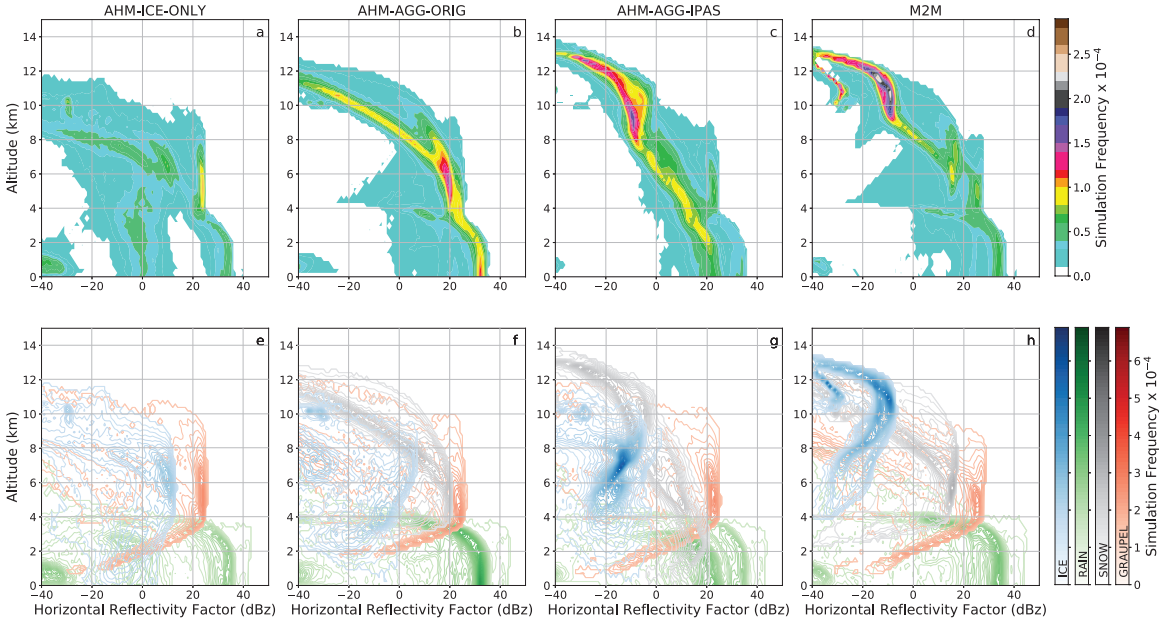


FIG. 14. CFADs of (a-d) total $Z_H$ and (e-h) contributions to $Z_H$ from ice (blue), rain (green), snow (grey), and graupel (red) for (a,e) AHM-ICE-ONLY, (b,f) AHM-AGG-ORIG, (c,g) AHM-AGG-IPAS, and (d,h) M2M. CFADs are generated for the entire domain and simulation time.





Accepted for publication in *Journal of the Atmospheric Sciences*. DOI 10.1175/JAS-D-20-0020.1.

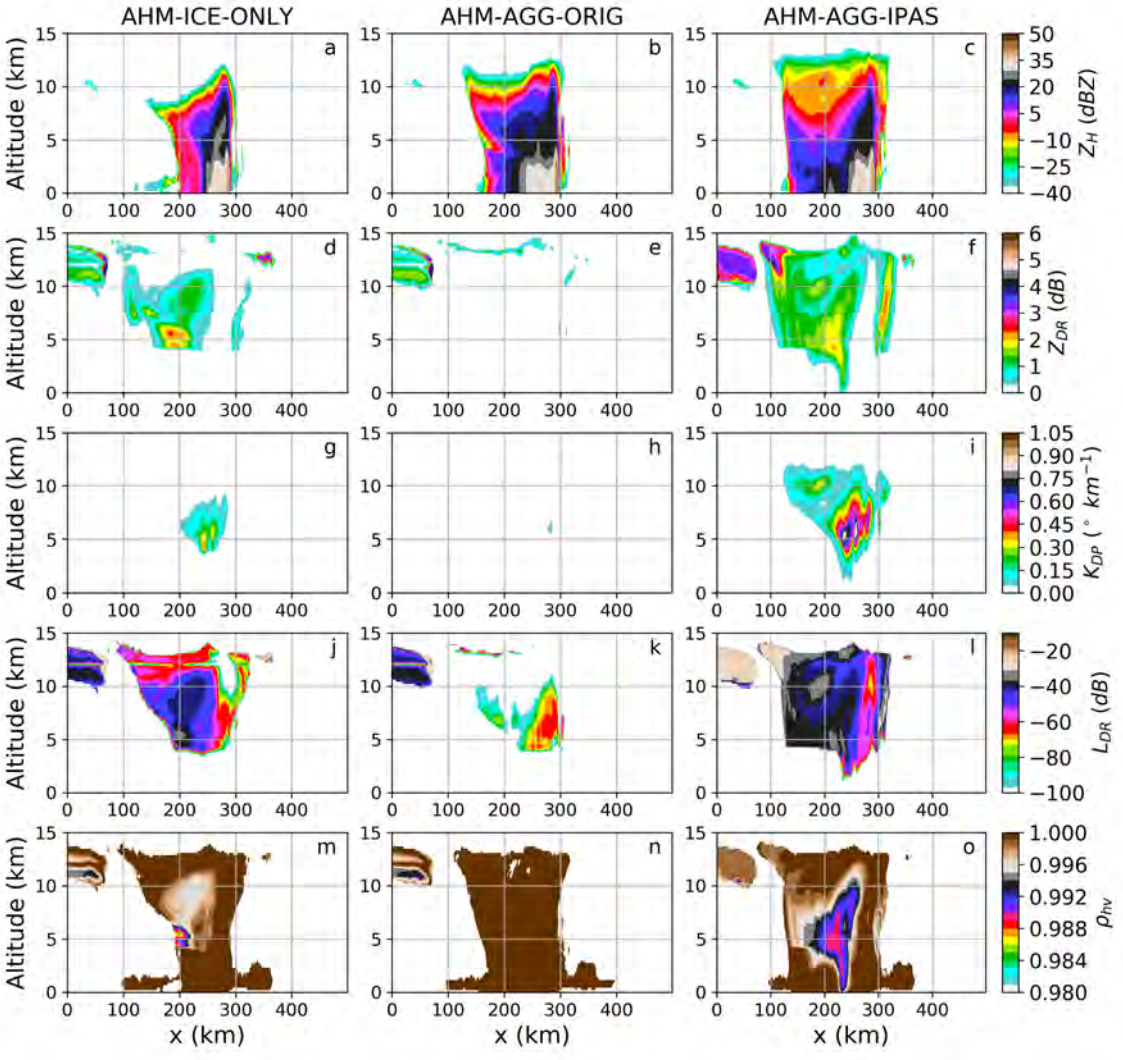


FIG. 15. Cross sections (averaged in the y-direction) of (a-c) reflectivity $Z_H$, (d-f) differential reflectivity $Z_{DR}$, (g-i) specific differential phase $K_{DP}$, (j-l) linear depolarization ratio $L_{DR}$, and (m-o) correlation coefficient $\rho_{hv}$ for AHM-ICE-ONLY, AHM-AGG-ORIG, and AHM-AGG-IPAS.



Accepted for publication in *Journal of the Atmospheric Sciences*. DOI 10.1175/JAS-D-20-0020.1.